

Turbulence-permitting air pollution simulation for the Stuttgart metropolitan area

Thomas Schwitalla*¹, Hans-Stefan Bauer¹, Kirsten Warrach-Sagi¹, Thomas Bönisch², Volker Wulfmeyer¹

¹ Institute of Physics and Meteorology, University of Hohenheim, Garbenstrasse 30, 70599 Stuttgart, Germany.

² High-Performance Computing Center Stuttgart (HLRS), Nobelstrasse 19, 70569 Stuttgart, Germany

Correspondence to: Thomas Schwitalla (thomas.schwitalla@uni-hohenheim.de)

Abstract. Air pollution is one of the major challenges in urban areas. It can have a major impact on human health and society and is currently a subject of several litigations at European courts. Information on the level of air pollution is based on near surface measurements, which are often irregularly distributed along the main traffic roads and provide almost no information about the residential areas and office districts in the cities. To further enhance the process understanding and give scientific support to decision makers, we developed a prototype for an air quality forecasting system (AQFS) within the EU demonstration project “Open Forecast”.

For AQFS, the Weather Research and Forecasting model together with its coupled chemistry component (WRF-Chem) is applied for the Stuttgart metropolitan area in Germany. Three model domains from 1.25 km down to a turbulence permitting resolution of 50 m were used and a single layer urban canopy model was active in all domains. As demonstration case study the 21 January 2019 was selected which was a heavy polluted day with observed PM₁₀ concentrations exceeding 50 µg m⁻³.

Our results show that the model is capable to reasonably simulate the diurnal cycle of surface fluxes and 2-m temperatures as well as evolution of the stable and shallow boundary layer typically occurring in wintertime in Stuttgart. The simulated fields of particulates with a diameter of less than 10 µm (PM₁₀) and Nitrogen dioxide (NO₂) allow a clear statement about the most heavily polluted areas apart from the irregularly distributed measurement sites. Together with information about the vertical distribution of PM₁₀ and NO₂ from the model, AQFS will serve as a valuable tool for air quality forecast and has the potential of being applied to other cities around the world.

1. Introduction

Currently more than 50 % of the global population live in cities whereas the United Nations (UN) expect a further increase by about 10 % in 2030 (UN, 2018). The UN also expect that in 2030 34% of the world population will reside in cities with more than 500 000 inhabitants.

Due to a strong increase of road traffic in major European cities (Thunis et al., 2017), pollution limits are often violated in larger cities. E.g. for particulate matter with particle diameters less than 10 µm (PM₁₀), the critical value is an annual mean concentration of 20 µg m⁻³ or a daily mean value of 50 µg m⁻³ (WHO, 2005). For Nitrogen dioxide (NO₂) the critical values are 200 µg m⁻³ and 40 µg m⁻³ as daily and annual mean values, respectively.

36 The violation of these pollution limits can lead to health and environmental problems and is currently part of several
37 litigations e.g. at the German Federal Administrative Court dealing with possible driving bans for non low-
38 emission vehicles. The basis for these litigations are mostly few local, unevenly distributed observations which .
39 In combination with special meteorological conditions like winter time thermal inversion layers it can be
40 misleading to conclude about the overall air quality in the city only from single observations. According to e.g.
41 the German Federal Immission Control Ordinance¹ it is sufficient that traffic related measurements are
42 representative for a section of 100 m, but this is not representative for the commercial and office districts in the
43 cities that are suffering from traffic control in case of fine dust alerts and residential areas. Namely in residential
44 areas health protection action plans require representative air quality measures.

45 Therefore, it becomes important to apply a more scientifically valid approach by applying coupled atmospheric
46 and chemistry models to predict air quality. Regional and global atmospheric models like the Weather Research
47 and Forecasting (WRF) model (Skamarock et al., 2019), the Consortium for Small Scale modeling (COSMO;
48 Baldauf et al., 2011), the Icosahedric Nonhydrostatic model (ICON; Zängl et al., 2015), or the Regional Climate
49 Model system (RegCM4; Giorgi et al., 2012) are often used to force offline chemistry transport models like
50 CHIMERE (Mailler et al., 2017), LOTOS-EUROS (Manders et al., 2017), EUROpean Air Pollution Dispersion
51 (EURAD; Memmesheimer et al., 2004), and Model for OZone And Related chemical Tracers (MOZART)
52 (Brasseur et al., 1998; Horowitz et al., 2003).

53 Several studies showed that combining an atmospheric model with an online coupled chemistry component is a
54 suitable tool for air quality and pollution modeling in urban areas at the convection permitting (CP) resolution
55 (Fallmann et al., 2014; Kuik et al., 2016; Zhong et al., 2016; Kuik et al., 2018; Huszar et al., 2020) .

56 Compared to chemical transport models, coupled models like WRF-Chem (Grell et al., 2005), COSMO-ART
57 (Vogel et al., 2009), ICON-ART (Rieger et al., 2015), and the Integrated Forecasting System (IFS) MOZART
58 (Flemming et al., 2015) allow for a direct interaction of aerosols with radiation leading to a better representation
59 of the energy balance closure at the surface as it would be the case when applying an offline chemistry model.

60 As usually the terrain and land cover over urban areas show fine scale structures which are not resolved even by a
61 CP resolution, there is a need for turbulence permitting (TP) simulations with horizontal grid increments of a few
62 hundred meters or even less. Important features are, e.g., urban heat island effects (Fallmann et al., 2014; Fallmann
63 et al., 2016; García-Díez et al., 2016; Li et al., 2019) and local wind systems like mountain and valley winds due
64 to differential heating (Corsmeier et al., 2011; e.g. Jin et al., 2016). Also, micro- and mesoscale wind systems can
65 develop due to urban structures and the heterogeneity of the land surface. It is well known that TP simulations are
66 a promising tool to further enhance the understanding of processes in the atmospheric boundary layer (Heinze et
67 al., 2017b; Panosetti et al., 2016; Heinze et al., 2017a; Bauer et al., 2020) in urban areas (Nakayama et al., 2012;
68 Maronga et al., 2019; Maronga et al., 2020).

69 In order to further enhance the quality of the simulations, building and urban canopy models (UCM) are developed
70 (Martilli et al., 2002; Kusaka and Kimura, 2004; Salamanca and Martilli, 2010; Maronga et al., 2019; Scherer et
71 al., 2019; Teixeira et al., 2019). The main purpose of UCMs is to provide a better description of the lower

¹https://www.gesetze-im-internet.de/bimschv_39/anlage_3.html

72 boundaries over urban areas such as building, roof and road geometries and their interactions with atmospheric
73 water vapor, wind, and radiation.

74 With the EU-funded project Open Forecast (<https://open-forecast.eu/en/>) it was intended to develop a prototype
75 for an air quality forecasting system (AQFS) for the Stuttgart metropolitan area in southwest Germany. Open
76 Forecast is a demonstration project to show the potential of open data combined with supercomputer resources to
77 create new data products for European citizens and public authorities. The long-term goal is to provide end users
78 and political decision-makers a useful tool, particularly considering further urbanization, heat island effects as well
79 as potential driving restrictions due to recent EU decisions on emission limits.

80 For our AQFS we use the WRF-Chem NWP model (Grell et al., 2005; Skamarock et al., 2019) as the WRF model
81 is extensively evaluated over Europe at different time scales and horizontal resolutions (San José et al., 2013;
82 Warrach-Sagi et al., 2013; Milovac et al., 2016; Lian et al., 2018; Molnár et al., 2019; Bauer et al., 2020; Coppola
83 et al., 2020; Schwitalla et al., 2020). It can easily be set up in a nested configuration over all regions of the Earth.
84 Compared to PALM-4U model, the nested model domains are driven by the full atmospheric and chemical
85 information from the parent domain along its lateral boundaries. Also, it contains well-characterized combinations
86 of parameterizations of turbulence and cloud microphysics in the outer domain that are consistent with the inner
87 TP domains where the high-quality cloud parameterization remains. No switch between different model systems
88 is required, which is expected to provide a great advantage with respect to the skill of air pollution and
89 meteorological forecasts.

90 To enhance the forecast skill, suitable variational and ensemble-based data assimilation systems are already in
91 place to further improve the meteorological initial conditions (Barker et al., 2012; Zhang et al., 2014; Kawabata et
92 al., 2018; Thundathil et al., 2020) and the chemical initial conditions (Chen et al., 2019; Sun et al., 2020) but this
93 is beyond the scope of our study.

94 The Parallelized Large-Eddy Simulation Model (PALM) model (Maronga et al., 2015) is another widely used TP
95 simulation model over Europe. PALM did not include the full interaction between land-surface, radiation, cloud
96 microphysics and chemistry during the performance of our study. The very recent version 6.0 of PALM-4U
97 (PALM for urban applications) (Maronga et al., 2020) is expected to contain a fully coupled chemistry module
98 (Khan et al., 2020).

99 Fallmann et al. (2016) and Kuik et al. (2016) performed air quality simulations with WRF-Chem over the cities of
100 Berlin and Stuttgart on a CP resolution down to 1km and less than 40 model levels. They used the TNO-MACC
101 emission inventory (Kuenen et al., 2014) which is available as an annual totals on a 7 km x 7 km resolution. As
102 the topography of Stuttgart is very complex, the AQFS applies the WRF-Chem model on a turbulence permitting
103 horizontal resolution using 100 model levels to account for the shallow boundary layer occurring during
104 wintertime. In addition, we applied a local emission data set from the Baden-Württemberg State Institute for the
105 Environment, Survey and Nature Conservation available as annual mean on a horizontal resolution of 500 m x 500
106 m to resolve fine-scale emission structures.

107 Our study focuses on the methodology how to set up a AQFS prototype by using WRF-Chem and its application
108 to a typical wintertime situation during January 2019 in the Stuttgart metropolitan area. The manuscript is set up
109 as follows: section 2 describes the design of our AQFS model system on the turbulence permitting resolution of

110 50 m followed by a description of the selected case study. Section 4 shows the results with respect to
111 meteorological variables and air quality including a discussion. Section 5 summarizes our work and provides an
112 outlook on potential future enhancements of the AQFS prototype.

113 2. AQFS design

114 2.1. WRF model set-up

115 For our AQFS prototype, we selected the Advanced Research WRF-Chem model in version 4.0.3 (Grell et al.,
116 2005; Skamarock et al., 2019). To reach the targeted resolution of 50 m, three model domains have been applied
117 with horizontal resolutions of 1250 m, 250 m, and 50 m and encompasses 800*800 grid cells in the outer domain
118 and 601*601 grid cells in the two inner TP domains. The reasons to start with a resolution of 1250 m in the
119 outermost domain is 1) to avoid the application of a convection parametrization which can deteriorate the model
120 results (Prein et al., 2015; Coppola et al., 2020), 2) that the model starts to partially resolve turbulent structures
121 whilst a PBL parametrization is still necessary (Honnert and Masson, 2014; Honnert et al., 2020), and 3) to reach
122 the target resolution with a nesting ratio of 5:1. The areas of model domain 1 and 3 are shown in Fig. 1.

123 As seen from Fig. 1b, the Stuttgart metropolitan area is characterized by an elevation variation of more than 300
124 m. The lowest elevation is approx. 220 m in the basin while the highest elevation reaches up to 570 m. As the main
125 traffic roads are in the basin, especially during wintertime this often leads to a worsening of the air quality as the
126 surrounding prevents an air mass exchange due to the stationary temperature inversion.

127 For the WRF model system land cover and soil texture fields are not available at resolutions higher than 500m.
128 Therefore we reclassified land cover data from the Copernicus CLC 2012 data set (European Union, 2012),
129 available on a resolution of 100 m, from the original 44 categories to the categories applied in the WRF model for
130 the simulations of the outer 2 domains. For the innermost model domain, we incorporated the most recent high-
131 resolution land-cover data set from the Baden-Württemberg State Institute for the Environment (LUBW), which
132 is derived from Landsat (Butcher et al., 2019) in 2010 and is available at 30 m resolution ([https://udo.lubw.baden-
133 wuerttemberg.de/public/](https://udo.lubw.baden-wuerttemberg.de/public/)) This data set was also reclassified to the corresponding land cover categories used in
134 WRF and is shown in Fig. 2.

135 The resolution of the provided default Food and Agriculture Organization of the United Nations (FAO) soil texture
136 data is only 10 km, therefore we used soil texture data from the International Soil Reference and Information
137 Centre (ISRIC) SoilGrids project (Hengl et al., 2014; Hengl et al., 2015). These data are available on a resolution
138 of 250 m. Terrain information was provided by the National Center for Atmospheric Research (NCAR) derived
139 from the Global multi-resolution terrain elevation data 2010 (GMTED2010) data set (Danielson and Gesch, 2011)
140 for domain 1. As the horizontal resolution of the GMTED2010 data set is 1 km, the 3" gap-filled Shuttle Radar
141 Topography Mission (SRTM) data set (Farr et al., 2007) is used for domain 2. As this resolution is still too coarse
142 for our targeted resolution of 50 m, the Digital Elevation model Europe (EU-DEM; European Union, 2017),
143 available at a resolution of 25 m, is used for the innermost domain.

144 In our set-up, we use 100 vertical levels for all domains using the traditional terrain following coordinate system
145 in WRF; 20 of the levels are distributed in the lowest 1100 m above ground level (AGL). All domains apply the
146 Noah-MP land surface model (Niu et al., 2011; Yang et al., 2011), the revised MM5 surface layer scheme based
147 on Monin-Obukhov similarity theory (Jiménez et al., 2012), the Thompson 2-moment cloud microphysics scheme

148 (Thompson et al., 2008) and the Rapid Radiative Transfer Model for GCMs (RRTMG; Iacono et al., 2008) for
149 parametrizing longwave and shortwave radiation. Due to the coarser resolution of the outermost domain, we
150 applied the Yonsei University (YSU; Hong et al., 2006) planetary boundary layer (PBL) parametrization in D01
151 only. As suggested by the WRF user guide, we applied the sub-grid turbulent stress option for momentum
152 (Kosovic, 1997) in domains two and three. The complete namelist settings are provided in the supplement.

153 The more sophisticated Building Effect Parameterization (BEP; Martilli et al., 2002) is not applied as this scheme
154 does not work with our selection of parametrizations. Instead, the single layer urban canopy model (UCM) (Kusaka
155 and Kimura, 2004) is selected to improve the representation of the urban canopy layer and the surface fluxes. The
156 parameters needed by the UCM are read in from the lookup table URBPARAM.TBL which was adjusted for the
157 Stuttgart area following Fallmann (2014).

158 Atmospheric chemistry is parametrized by the Regional Acid Deposition Model 2nd generation (RADM2) model
159 (Stockwell et al., 1990). RADM2 features more than 60 chemical species and more than 135 chemical reactions
160 including photolysis. Aerosols are represented by the Modal Aerosol Dynamics Model for Europe (MADE) and
161 Secondary Organic Aerosol Model (SORGAM) scheme (Ackermann et al., 1998; Schell et al., 2001) considering
162 size distributions, nucleation, coagulation, and condensational growth. The combination of RADM2_MADE-
163 SORGAM is a computationally efficient approach and is widely used for simulations over Europe (Forkel et al.,
164 2015; Mar et al., 2016). To further enhance vertical mixing of CO to higher altitudes during nighttime over urban
165 grid cells, the if-statements in the dry deposition driver of WRF-Chem at lines 690 and 707 have been deleted
166 according as shown in the supplement of Kuik et al. (2018).

167 Compared to a previous study from (Fallmann et al., 2016), who performed simulations over the Stuttgart
168 metropolitan area using WRF-Chem on a CP resolution of 3 km, or the study of (Kuik et al., 2016) who performed
169 a three month simulation at different resolutions over Berlin, simulations on the TP resolution provide a much
170 more realistic representation of the land-cover structures (see Fig. 2 in this paper and e.g. Fig. 2b in Fallmann et
171 al. (2016)). As the climate in the Stuttgart metropolitan area is strongly influenced by the topography, we are
172 convinced that our special combination of a TP resolution and high-resolution emission data (see section 2.3) will
173 lead to a better understanding and prediction of the air pollution situation in this area.

174 Currently, air pollution modeling with WRF-Chem is a computationally expensive task. Depending on the number
175 of output variables and frequency (5 min in our study), a 24 h simulation currently takes around 36 h wall clock
176 time. For future experiments it is worth to try the I/O quilting option in combination with PNetCDF which should
177 considerably reduce the time spent on I/O.

178 While the WRF model itself is ready for hybrid parallelism (MPI + OpenMP), the WRF-Chem model can only be
179 used with MPI. If WRF-Chem could be enhanced for additional OpenMP capabilities, this would lead to an
180 increase in computation speed almost linear with the number of OpenMP threads.

181 Due to the complexity of the chemistry model in combination with the very high horizontal resolution and the
182 calm meteorological conditions, the adaptive model time step option was chosen instead of a fixed time step.
183 Model output is available in 5 min intervals for the innermost model domain.

184 Our single day case study on the turbulence permitting (TP) scale is designed to serve as a test bed to set up an air
185 quality forecasting system prototype for the Stuttgart metropolitan area. For process studies, the model chain itself

186 can be applied to other areas over the globe as long as 1) detailed land cover and soil texture data are available, 2)
187 high-resolution emission data not only from traffic are available. The new model system can be even applied in a
188 forecast and warning mode, if near real-time emissions as well as meteorological and chemical input data are
189 available in a timely manner. As the computational demands of applying WRF-Chem on the TP scale are very
190 high, access to an HPC system is a prerequisite.

191 **2.2. Model initialization**

192 The meteorological initial and boundary conditions were provided by the operational ECMWF integrated
193 forecasting system (IFS) analysis on model levels. The IFS is a global model with 9 km horizontal resolution and
194 applies a sophisticated four-dimensional variational (4DVAR) data assimilation system (Bonavita et al., 2016).
195 The data have been retrieved from the ECMWF Meteorological Archival and Retrieval System (MARS) and were
196 interpolated to a resolution of 0.05°.

197 The initialization and provision of the boundary conditions of the chemistry of the model is done with data from
198 the Whole Atmosphere Community Climate Model (WACCM; Marsh et al., 2013) using the Model for Ozone and
199 Related Chemical Tracers (MOZART) conversion tool MOZBC (Pfister et al., 2011). As the resolution of
200 WACCM is very coarse, the input data was enhanced by the ECMWF Copernicus Atmosphere Monitoring Service
201 (CAMS) reanalysis data set on 60 model levels and 40 km horizontal resolution (Inness et al., 2019).

202 **2.3. Emission data**

203 The emission data set used in this study is a combination of three products. Global input data sets containing coarse
204 resolution emissions from different sources are obtained from the BRAMS numerical modeling system (Freitas et
205 al., 2017). The PREP-CHEM-SRC tool (Freitas et al., 2011) is then applied as pre-processor to convert these
206 emissions to the appropriate WRF units and interpolate the data onto the WRF model grid.

207 As global emission data sets have a very coarse resolution in space and time, higher resolution emission data for
208 Europe from the Copernicus Atmosphere Monitoring Service (CAMS; Copernicus) CAMS-REG-AP product
209 became available (Granier et al., 2019). Its resolution is approx. 7x7 km and it is based on total annual emissions
210 from 2016. This product provides emissions of PM₁₀, PM_{2.5}, SO₂, CO, NO_x, and CH₄ and contains sources from
211 different sectors, separated into ten different categories following the Gridded Nomenclature For Reporting
212 (GNFR; Granier et al., 2019).

213 The third emission data set (BW-EMISS) deployed in our study was obtained from the Baden-Württemberg State
214 Institute for the Environment (LUBW). This data set contains annual mean emissions from different sectors
215 following the GNFR classification and is currently available only until 2014 and has a horizontal resolution of 500
216 m. Unfortunately, more recent quality-controlled data sets were not available when our study was performed. It is
217 expected that annual emissions for 2018 will become available by mid of 2021.

218 As CAMS-REG-AP and BW-EMISS only contain annual sums or annual mean values, a temporal decomposition
219 was applied for both data sets following Denier van der Gon et al. (2011). Depending on the GNFR code, the data
220 are first projected onto the corresponding month, followed by the corresponding day of the week and the hour of
221 the day. A similar approach was performed e.g. in Resler et al. (2020, under review) for the city of Prague. After

222 finishing the decomposition, the data are converted to the corresponding units and interpolated onto the WRF
223 model grid using the Earth System Modeling Framework (ESMF; Valcke et al., 2012) interpolation utilities.

224 Figure 3 shows an example of the NO₂ emissions derived from the CAMS-REG-AP product (left) and the emission
225 data derived from the LUBW data set (right) on January 21, 2019 at 07 UTC.

226 Due to its much higher horizontal resolution, the BW-EMISS data set (Fig. 3b) shows much more detailed
227 structures for the NO₂ emissions which are mainly caused by road traffic. The average emissions for this particular
228 time step are 2 mol km⁻² h⁻¹ for the CAMS-REG-AP data set and 7 mol km⁻² h⁻¹ for the BW-EMISS data set.

229 In addition, the following adjustments have been performed: 1) NO_x emissions from forest grid cells have been
230 reduced by 90 %, 2) Road traffic NO_x emissions were transformed into 90 % NO and 10 % NO₂ emissions
231 following Kuik et al. (2018) 3) All emissions from Stuttgart airport were reduced by 90 % during the nighttime
232 flight ban between 00 UTC and 04 UTC as well as after 21 UTC.

233 The WRF-Chem model only ingests one emission data set per species, hence emissions from the different GNFR
234 categories have been accumulated to a single emission data set before performing the simulation. Figure 4
235 summarizes all necessary steps and the complete data and workflow of the AQFS prototype.

236 2.4. Observations

237 We used data from three meteorological stations (Stuttgart-Schnarrenberg (48.8281°N 9.2°E, elevation 314 m),
238 Stuttgart Airport (48.6883°N 9.2235°E, elevation 375 m), and Institute of Physics and Meteorology (IPM) at the
239 University of Hohenheim (48.716°N 9.213°E, elevation 407 m) to validate the simulated 2m temperatures; data
240 are available every 10 minutes. The locations are indicated by the black dots in Fig. 1b. In addition, the radiosonde
241 data from Stuttgart-Schnarrenberg were used.

242 3. Case study description

243 For our study, we selected 21 January 2019. This day was characterized as “fine dust alarm” situation (Stuttgart
244 Municipality and German Meteorological Service (DWD), 2019) which is defined by a combination of the
245 following criteria:

- 246 1. Expected daily maximum PM₁₀ concentration at Stuttgart Neckartor (NT in Fig. 1b) is higher than 30 μg
247 m⁻³
- 248 2. No rain on the following day
- 249 3. 10-m wind speed less than 3 m s⁻¹ from south to northwest directions (180-330 °)
- 250 4. Nocturnal atmospheric inversion
- 251 5. Mixing layer depth less than 500 m during the day
- 252 6. Daily average 10-m wind speed less than 3 m s⁻¹ from all directions

253 A sufficient criterion is a higher PM₁₀ concentration following (1). If (1) is not fulfilled, then (2) and (3) together
254 with either (4) and/or (5) has to be fulfilled. If only (4) or (5) is fulfilled, then (6) has to be considered. For our
255 case study, the criteria 1-5 were fulfilled.

256 The thick lines in Fig. 5 shows the observed PM₁₀ and NO₂ concentrations at several stations in our model domain.
257 From Fig. 5a the high NO₂ concentrations at Neckartor and Hohenheimer Strasse occurring after sunrise can be

258 clearly identified. While these measurements are taken next to main roads, the other stations show considerably
259 lower NO₂ concentrations throughout the day. The PM₁₀ concentrations (Fig. 5b) show extremely high values at
260 Neckartor exceeding 100 µg m⁻³ around noon time and the evening rush hour which clearly meets the main criteria
261 of the “fine dust alarm situation”. The other stations, which are not directly taken near main roads with heavy
262 traffic show considerably lower PM₁₀ concentrations around 40 µg m⁻³.

263 This day was a typical winter weather situation. Central Europe was located at the east flank of a blocking high
264 pressure system located over the East Atlantic together with moderate to low horizontal geopotential gradients and
265 resulting weak winds at 500 hPa in southwestern Germany (Fig. 6a).

266 Near surface temperatures are below freezing level, between 1000 and 850 hPa very light easterly winds
267 characterize the flow, and a dry layer is present around 925 hPa (Fig. 6b). Above 850 hPa, the wind direction
268 rapidly changes to westerly directions, but the wind speeds remain below 5 m s⁻¹ (see Fig. 7a).

269 The inversion between the two air masses inhibits vertical mixing leading to higher concentrations of aerosols in
270 the lowest few hundred meters above ground (AGL) and preventing air mass exchange aloft. This inversion is
271 further enhanced by the special orography of Stuttgart city (see later Fig. 15).

272 4. Results and Discussion

273 4.1. Meteorological quantities

274 Figure 7a shows a Skew-T diagram of the model initial conditions (black line) at Stuttgart-Schnarrenberg valid at
275 00 UTC 21 January 2019 in comparison with the observations (red line).

276 The initial conditions agree well with the sounding showing a weak temperature inversion around 900 hPa with
277 high relative humidity values up to 650 hPa. The observed and simulated lifting condensation level is 940 hPa and
278 the integrated water vapor (PWAT) is 8 mm. Wind speed and direction agree with the observations showing a
279 wind shear above 850 hPa associated with low wind speeds of less than 5 m s⁻¹.

280 To further evaluate the stratification conditions during the day, Figure 7b shows the observed and simulated
281 temperature, dew point, and wind profiles at 11 UTC. The vertical structure of the observation and the simulation
282 has an almost perfect agreement. The temperature inversion layer at 910 hPa is well captured although the
283 simulated temperatures below the inversion are too high by about 1.5 K. The humidity profile (expressed as
284 dewpoint profile) is also very well captured with the largest moisture content below 870 hPa. Wind speed and
285 direction above 850 hPa agree well with the observation throughout the atmosphere. In regard of the vertical model
286 resolution, the wind situation in the lowest 1000 m AGL is also reasonably represented.

287 Figure 8 exemplarily shows the simulated 2-m temperature together with 10-m wind velocities at 12 UTC (noon
288 time) to display the complexity of the Stuttgart metropolitan area.

289 The 2-m temperatures show a daytime warming of downtown Stuttgart and the Neckar Valley while still
290 temperature slightly below 0°C are present at higher elevations (blue colors in Fig. 8). The wind situation is very
291 complex due to weak wind speeds in combination with a shallow boundary layer (see later Fig. 16) but the wind
292 flow along the upper Neckar river (south of 48.75°) is strongly pronounced. After sunset, wind speed starts to
293 decrease and the channeling effect along the Neckar weakens (not shown).

294 Figure 9 shows an evaluation of the diurnal cycle of 2-m temperatures at the three measurement sites
295 Schnarrenberg, IPM and airport. Sunrise is at 07 UTC and sunset at 16 UTC and the model data are averaged over
296 5 grid cells around the measurement site to take into account that even a simulation with 50 m resolution cannot
297 fully capture the local conditions at the measurement site. The northern station Schnarrenberg shows a lower
298 temperature throughout the day than the other two stations, which are situated 3 km apart at a similar elevation.
299 The temperature is about 1 K colder during the day and 0.5 K colder during the night.

300 At Schnarrenberg, the observed diurnal cycle is reasonably well simulated with WRF. Between 00 and 15 UTC, a
301 warm temperature bias of 1 K is present in the simulation, which turns into a small negative bias after sunset. At
302 IPM, the simulation shows a cold bias until 04 UTC turning into a warm bias as the strong temperature drop is not
303 simulated until 06:30 UTC. After 09 UTC until sunset the simulated temperature agrees well with the observations
304 while later a cold bias of around 1 K is present.

305 For the airport station, the model stays too warm with a positive bias of almost 2 K between 05 and 09 UTC.
306 During the further course of the day, the bias reduces to 1 K at noon while after sunset it turns into a negative bias
307 of 1 K.

308 A possible reason for the larger differences at the airport and IPM before (after) sun rise (sun set) is the observed
309 occurrence of low stratus or fog. At the beginning of the simulation, cloud coverage was reported by 5—7 octas
310 (broken clouds) over Schnarrenberg and the airport at approx. 500 m AGL (not shown) while after 04 UTC the
311 low level clouds started to diminish at Schnarrenberg first leading to a strong cooling until the early morning which
312 is seen as a temperature decrease in the observations shown in Fig. 9. The temperature drop at Schnarrenberg and
313 IPM is also simulated but with a delay of approx. 2 h. A reason for this delayed temperature drop could be a
314 simulated thin cloud layer around 1000 m AGL which is present in the lower left and partly the lower right quadrant
315 of the model domain. This cloud layer slowly moves in a southeasterly direction and starts to dissolve around 06
316 UTC.

317 During the evening transition and the following night, the low stratus is developing again at the measurement sites
318 with a ceiling of 500 m AGL but is not simulated and thus contributes to a stronger cooling in the model. Another
319 contributing factor to the delayed cloud dissipation could be the turbulence spin-up time (Kealy et al., 2019), but
320 this is beyond the scope of this study.

321 Although no measurements of sensible heat and ground heat fluxes are available, diurnal cycles of the fluxes at
322 the locations IPM, Schnarrenberg, airport, and Schlossplatz were investigated. Figure 10 shows the simulated
323 surface sensible heat and ground heat flux at the four sites.

324 The sensible heat flux (Fig. 10a) shows a typical diurnal cycle with fluxes around zero before (after) sunrise
325 (sunset). During the day, the model simulates typical wintertime sensible heat fluxes between 40 and 100 W/m²
326 (e.g. Zieliński et al., 2018), which nicely shows a dependency on the different underlying land cover types. Lower
327 sensible heat fluxes occur over the sparsely vegetated surface at the airport as compared to the cropland station
328 IPM while the urban locations Schnarrenberg and Schlossplatz shows interjacent values. As the algorithm to
329 diagnose the 2-m temperature in NOAHMP is rather complex, no clear correlation between SH and the 2-m
330 temperature shown in Fig. 9 can be made. The latent heat fluxes (not shown) are almost zero at Schnarrenberg and
331 less than 10 W m⁻² at the other two locations due to cold and dry winter conditions

332 The simulated ground heat flux (Fig. 10b) shows an interesting behavior. Until sunrise, the simulated GRDFLX at
333 the airport and IPM shows fluctuations around -50 W m^{-2} indicating some low levels clouds in accordance with
334 the too high simulated 2-m temperatures shown in Fig. 9. During the further course of the day, IPM and airport
335 show a clear diurnal cycle with maximum values between 100 and 170 W m^{-2} reflected in the highest surface
336 temperatures during the day (not shown).

337 At Schnarrenberg, most of the time the ground heat flux is less than zero indicating a cooling of the soil, while
338 between 12 UTC and 16 UTC small positive values are simulated. As Schnarrenberg is categorized as low density
339 residential (category 31) with an urban fraction of 0.5 and the UCM is applied here, energy is mainly stored in the
340 urban canopy layer instead of being transferred into the soil. At Schlossplatz (high-density residential) the ground
341 heat flux shows a similar shape but with a larger amplitude as compared to Schnarrenberg.

342 As this day was characterized by a shallow PBL and a temperature inversion, it is worth to investigate the PBL
343 evolution during the day. Figures 11a, b show time-height cross sections of potential temperature at IPM (top) and
344 Schnarrenberg (bottom).

345 Both locations are characterized by a very stable shallow boundary layer until 09 UTC with a depth of less than
346 200 m. Between 03 and 09 UTC the temperatures at Schnarrenberg are up to 1.5 K colder near the surface (Fig. 9)
347 resulting in a stronger potential temperature gradient up to 400 m AGL compared to the IPM location. During the
348 day, the boundary layer height increases to 400 m above ground as indicated by the constant potential temperature
349 (e.g. Bauer et al., 2020) which is a typical value for European winter conditions (Seidel et al., 2012; Wang et al.,
350 2020). The PBL heights are also visible by the potential temperature gradients ($\Delta\theta$) shown in Figs. 11c, d. During
351 the morning hours, a very shallow boundary layer was simulated at Schnarrenberg (blue colors in Fig. 11c) while
352 at IPM some fluctuations are present. During daytime, $\Delta\theta$ nicely shows the PBL height evolution up to 400 m
353 AGL, while after sunset the PBL collapses to a very stable layer again (dark blue colors in Figs. 11c, d) with
354 heights between 50—100 m AGL. Calculating the gradient Richardson number (Ri ; Chan, 2008) (not shown) and
355 assuming a threshold of 0.25 for a turbulent PBL (Seidel et al., 2012; Lee and Wekker, 2016) leads to similar
356 results After sunset around 15:30 UTC the boundary layer collapses to a night-time stable boundary layer and a
357 temperature inversion occurred again.

358 **4.2. Evaluation of NO_2 and PM_{10}**

359 The most relevant air pollutants for air quality considerations in cities are NO_2 and PM_{10} . Sources for these are
360 mainly truck supply, transit, and commuter traffic through the city as well as advection from motorways south,
361 west, and northwest of Stuttgart.

362 As the incorporated emissions are from 2014 and are based on annual values, it cannot be expected that the model
363 exactly matches the observed concentrations. For instance, the actual traffic, the sequence of traffic lights and
364 traffic congestions of this particular day cannot be realistically represented. In addition, all diagnosed or prognostic
365 chemical quantities are only available on model levels. For TP applications with WRF, selecting the lowest model
366 half level being at $\sim 15 \text{ m}$ above ground is a reasonable choice (Bauer et al., 2020).

367 We start with the discussion of the simulated horizontal distributions followed by vertical cross sections of NO_2
368 and PM_{10} .

369 4.2.1 Horizontal distribution

370 Figure 12 shows the horizontal distribution of the NO₂ concentration at the lowest model half level (~15 m AGL)
371 at the four timesteps 07:30 UTC, 12 UTC, 18 UTC and 23 UTC 21 January 2019.

372 At 7:30 UTC the morning traffic rush hour is visible in the NO₂ concentrations in Fig. 12a. High NO₂
373 concentrations of more than 80 µg m⁻³ are simulated along the motorway A81 in the northwest of the domain, over
374 the airport and over downtown Stuttgart. In the Neckar Valley the concentrations exceed 120 µg m⁻³. At noon time
375 (Fig. 12b), when turbulence is fully evolved (Fig. 11), the simulated NO₂ concentrations are less than 30 µg m⁻³
376 on average apparently due to vertical mixing of NO₂ (see next section). In the evening (Fig. 12c) the simulated
377 NO₂ concentrations increase again showing values of more than 100 µg m⁻³ over the airport and more than 150 µg
378 m⁻³ in downtown Stuttgart and the Neckar Valley due to road and air traffic. The high morning concentrations
379 along the northwestern motorway are not reached since the wind speed increases and the near surface winds turn
380 towards a westerly direction. According to the emission data set converted by the temporal factors, the evening
381 traffic spreads over a longer time. During the night (Fig. 12d), NO₂ accumulates in the Stuttgart basin as well as
382 the Neckar Valley due to the very low nocturnal boundary layer height of less than 200 m capped by an atmospheric
383 inversion (Fig. 11).

384 Compared to the observed NO₂ concentrations (Fig. 5a), the simulated concentrations during the peak traffic times
385 are too high at Arnulf-Klett Platz, Neckartor and Hohenheimer Strasse. Possible reasons are that either the traffic
386 is reduced and/or that the vehicle emission classification have been improved since 2014. Another contributing
387 factor could be that the vertical mixing near the surface is too weak during sunrise and sunset while it appears
388 slightly too strong during daytime as indicated by the very low simulated NO₂ concentrations.

389 Apart from NO₂, the concentration of PM₁₀ is an important parameter for air quality considerations and is the
390 decisive factor for proclaiming a “fine dust alarm” situation in Stuttgart (Stuttgart Municipality and German
391 Meteorological Service (DWD), 2019).

392 Figure 13 shows the horizontal distribution of PM₁₀ for the same time steps as shown in Fig 12.

393 During the morning traffic (Fig. 13a), PM₁₀ accumulates in the Stuttgart basin as this is an area with heavy traffic
394 during the morning and an atmospheric inversion is present (Fig. 7). Interestingly, the high NO₂ concentrations
395 along the motorway (Fig. 12a) do not lead to very high PM₁₀ concentrations potentially due to chemical transitions
396 caused by low temperatures.

397 During daytime when turbulence is fully evolved, the concentration of PM₁₀ decreases to less than 20 µg m⁻³ due
398 to vertical mixing and horizontal transport (see next section). After sunset (Fig. 13c) PM₁₀ starts to accumulate
399 again in the Stuttgart basin showing concentrations between 35—40 µg m⁻³. During the night (Fig. 13d) PM₁₀
400 accumulates over a large part of the model domain as the nocturnal boundary layer is very shallow, an inversion
401 layer is present 200 m AGL and the wind direction changes from north to west. In the configuration we use in our
402 study, PM₁₀ is a diagnostic variable which is a sum of the PM_{2.5} concentration (which is around 26 µg m⁻³ at 23
403 UTC) and the other prognostic aerosol species. As the night is very cold with temperatures far below freezing and
404 the humidity is very high, the high concentrations could imply a very (too) strong deposition or be the result of a
405 combination of dense evening traffic and fog formation due to weak near-surface winds.

406 4.2.2 Vertical distribution of NO₂ and PM₁₀

407 In addition to the horizontal distribution of near surface NO₂ and PM₁₀, TP simulations with a fine vertical
408 resolution also enable qualitative insights into the vertical distribution of pollutants. Figure 14 shows West-East
409 cross sections at Neckartor (Fig. 1b) during the morning rush hour and at noon time. Neckartor is one of the
410 heaviest traffic locations in the Stuttgart city area.

411 The NO₂ concentration during the morning rush hour shows an accumulation along the motorway (red arrow in
412 Fig. 14a) and in the region around Neckartor (white arrow in Fig. 14a) with concentrations exceeding 100 µg m⁻³
413 as the atmospheric inversion prevents exchange with the layers above (Fig. 7). The vertical extent of concentrations
414 higher than 30 µg m⁻³ is about 200 m AGL with a strong reduction above.

415 During noon time (Fig. 14b), the simulated NO₂ concentration is much lower (less than 30 µg m⁻³) as turbulence
416 leads to a stronger mixing throughout the boundary layer up to 400 m AGL which is in accordance with the
417 simulated potential temperature timeseries shown in Fig. 11.

418 Figure 15a displays the simulated PM₁₀ concentrations during the morning rush hour. Similar like for NO₂, higher
419 concentrations of more than 25 µg m⁻³ is simulated along the motorway and in the Stuttgart basin. During the day,
420 PM₁₀ is vertically mixed showing a clear gradient around 800 m above sea level (ASL) (Fig. 15b) while
421 concentrations remain between 10-20 µg m⁻³ within the boundary layer.

422 Apart from the West-East cross sections it is also worthwhile to investigate the vertical temporal evolution of NO₂
423 and PM₁₀ concentrations. Therefore, Fig. 16 shows time height cross sections of NO₂ (top) and PM₁₀ (bottom) at
424 Neckartor.

425 Well visible are the high simulated NO₂ and PM₁₀ concentrations during the morning rush hour with peak values
426 of more than 120 µg m⁻³ NO₂ and more than 40 µg m⁻³ PM₁₀. The high concentrations of NO₂ and PM₁₀ are present
427 up to around 150-200 m AGL. During daytime, turbulence efficiently mixes the pollutants up to higher altitude
428 and the near surface concentrations are quickly reduced. During the evening when the very shallow boundary layer
429 has developed again and evening traffic commences, the particle concentrations increase, and peak values of more
430 than 30 µg m⁻³ are simulated below 100 m AGL.

431

432 5. Summary and conclusion

433 This paper describes the setup of an AQFS prototype using WRF-Chem for the Stuttgart Metropolitan area.
434 Because of the complex topography in this region, this simulation system requires a very high horizontal resolution
435 down to the turbulence-permitting scale to represent all orographic and land cover features.

436 For the development of this prototype 21 January 2019 served as test case as this was a typical winter day with an
437 atmospheric inversion. In addition, this day was characterized as “fine dust alarm” situation where the PM₁₀
438 concentration at the station Neckartor in the Stuttgart basin was expected to exceed 30 µg m⁻³
439 (http://www.stadtklima-stuttgart.de/stadtklima_filestorage/download/luft/Feinstaubwerte-2019_AN.pdf). The
440 model setup encompassed three domains down to a turbulence permitting resolution of 50 m.

441 The initial conditions were provided by the ECMWF operational analysis, the CAMS reanalysis and WACCM
442 model for background chemistry. Emission data sets from CAMS-REG-AP and high-resolution data with 500 m
443 resolution from LUBW were combined to be used in the AQFS. As current emission data sets only provide annual
444 totals or means, a temporal decomposition following TNO was applied (Denier van der Gon et al., 2011).

445 For this case study, we focused on the results with respect to 2-m temperature, surface fluxes and boundary layer
446 evolution as well as horizontal and vertical distributions of NO₂ and PM₁₀.

447 Our results revealed that despite the complex topography in Stuttgart, the model is in general capable to simulate
448 a realistic diurnal cycle of 2-m temperatures although, compared to observations, differences of up to 1 K occur.
449 Apparently the model has difficulties with the dissolution of low stratus clouds between 03 and 06 UTC which
450 was also reported in the work of Steeneveld et al. (2015) resulting in a warm 2-m temperature bias during the
451 morning. Although no measurements are available, the surface sensible heat fluxes show a clear diurnal cycle with
452 the magnitude clearly depending on the underlying land cover type. The low simulated ground heat flux and its
453 fluctuations between 00 UTC and sunrise partially confirm the fog dissolution issue but more test cases are needed
454 for a more detailed investigation. Over grid cells where the single layer UCM is active, most of the ground heat
455 flux is stored in the canopy layer thus not transferred into the soil. The high vertical resolution of 100 levels enables
456 a realistic representation of the nocturnal and daytime temperature inversion with an accompanying shallow
457 boundary layer of less than 400 m during the day.

458 The simulation of PM₁₀ shows an exceedance of the 30 µg m⁻³ concentration threshold close to the Neckartor
459 station and also fulfills the other fine dust alarm criteria shown in section 3. Compared to the usually unevenly
460 distributed air quality measurements, the AQFS allows further insights into the spatio-temporal pollutant
461 distribution. The horizontal distributions of NO₂ and PM₁₀ at this particular day clearly indicate the main polluted
462 areas along the motorways and in the Stuttgart basin. The special orography of Stuttgart with its basin favors the
463 accumulation of NO₂ and PM₁₀ in the morning and evening while the pollutants are well mixed to around 200-400
464 m AGL when the boundary layer is fully evolved.

465 The simulation also shows that pollutants can be advected from the motorway A81 towards Stuttgart, depending
466 on the wind situation, potentially leading to an increase of the NO₂ and partially PM₁₀ concentrations in the
467 Stuttgart basin. As can be seen from Figs. 12 and 13, the Neckar Valley can also have a large impact on the
468 pollutant concentration in the Stuttgart basin in case an atmospheric inversion together with prevailing easterly
469 winds is present.

470 This is, to our knowledge, the first study of applying WRF-Chem on a TP resolution for an urban area. To derive
471 more robust conclusions with respect to air pollution, more cases studies with different weather situations during
472 winter and summer time are necessary. Nevertheless, our evaluation gives the following indications to further
473 improve the quality of such simulations:

- 474 I. Applying high spatial and temporal resolution gridded emission data from all pollution sources in near
475 real-time to avoid extrapolating annual emissions to individual days. This will help to enhance the
476 simulation of the diurnal cycles of chemical species.
- 477 II. Improving the chemical background e.g. by applying higher resolution products from the CAMS
478 European Air quality project (Marécal et al., 2015). This will help to have a more detailed structure of
479 the chemical constituents beneficial for subsequent downscaling simulations.
- 480 III. Using a longer spin-up period and applying a larger TP model domain to further improve the spin-up of
481 turbulence in the model
- 482 IV. Considering vertical distribution of surface emissions (e.g. Bieser et al., 2011; Guevara et al., 2020)
- 483 V. Considerably increase the number of pollutant measurements to allow more robust conclusions

484 The AQFS has a great potential for urban planning applications. For example, land cover could be changed from
485 urban low density to urban high density to investigate the impact of urban re-densification e.g. on temperature and
486 air quality. Although no BEP can be applied on the TP resolution with our combination of parameterizations,
487 changes of the parameters required for the single layer UCM offer the opportunity to perform sensitivity analysis
488 with respect to different building heights, urban greening effects (Fallmann et al., 2016), or anthropogenic heating
489 (Karlický et al., 2020). Recently, Lin et al. (2020) developed an interface to use output from high-resolution WRF
490 simulations to force PALM 6.0 in an offline mode which could be another tool in the future to study microscale
491 structures in urban areas.

492 In the future, more emphasis should also be put on an improvement of the I/O (e.g. by means of quilting) and
493 additional OpenMP capabilities in WRF-Chem. However simulations with WRF-Chem at the TP resolution will
494 still require around 1500-2000 compute cores for operational use due to the small numerical time step necessary.

495 Although air quality modeling on the TP scale is a very challenging and computationally expensive task, we are
496 convinced that the AQFS will have a great potential to further improve process understanding and will certainly
497 help politicians to make decisions on a more scientifically valid basis.

498 **Code and data availability**

499 The WRF-Chem code version 4.0.3 can be downloaded from [https://github.com/wrf-](https://github.com/wrf-model/WRF/archive/v4.0.3.tar.gz)
500 [model/WRF/archive/v4.0.3.tar.gz](https://github.com/wrf-model/WRF/archive/v4.0.3.tar.gz). ECMWF analysis data can be obtained from [https://apps.ecmwf.int/archive-](https://apps.ecmwf.int/archive-catalogue/?type=an&class=od&stream=oper&expver=1)
501 [catalogue/?type=an&class=od&stream=oper&expver=1](https://apps.ecmwf.int/archive-catalogue/?type=an&class=od&stream=oper&expver=1) (last access: 26 August 2020). The user's affiliation needs
502 to belong to an ECMWF member state to benefit from these data sets. Due to restrictions on the input data sets for
503 this simulation, the data can only be made available upon special request from the corresponding author.

504 **Author Contributions**

505 TS prepared all emission data, set up the model and performed the simulation supported by HSB. HSB reclassified
506 the CORINE land use data set. KWS and TB conceived the idea and coordinated the project with VW. TS prepared
507 all figures and wrote the manuscript with input from all authors. All authors equally contributed to the scientific
508 discussion and helped to shape the research.

509 **Video Supplement**

510 The video shows the simulated diurnal evolution of the NO₂ concentration (Schwitalla, 2021a) and PM₁₀
511 concentration (Schwitalla, 2021b) over the Stuttgart metropolitan area.

512 **Competing interests**

513 The authors declare that they have no conflict of interest.

514 **Acknowledgements**

515 This study has been performed within the EU-funded project *Open Forecast* (Action number 2017-DE-IA-0170).
516 We acknowledge ECMWF for providing analysis data from the operational IFS and CAMS reanalysis. The
517 Emissions of atmospheric Compounds and Compilation of Ancillary Data (ECCAD) system is acknowledged for
518 providing the CAMS-REG-AP Emission data set. We acknowledge the use of the WRF-Chem preprocessor tool

519 MOZBC, provided by the Atmospheric Chemistry Observations and Modeling Lab (ACOM) of NCAR. The
520 Baden-Württemberg State Institute for the Environment (LUBW) is highly acknowledged for providing high-
521 resolution annual emission data and for the high-resolution land cover data. Joachim Ingwersen from the
522 Department of Biogeophysics at the University of Hohenheim is acknowledged for converting the soil texture data.
523 Joachim Fallmann from the University of Mainz is acknowledged for providing the necessary code enhancement
524 of the dry deposition driver module to correctly couple the urban canopy model. The simulation was performed
525 on the national supercomputer Cray XC40 Hazel Hen at the High Performance Computing Center Stuttgart
526 (HLRS) within the WRFSCALE project. We acknowledge the editor Ronald Cohen and both anonymous referees
527 for their valuable comments to improve the quality of the paper.

528 References

- 529 Ackermann, I. J., Hass, H., Memmesheimer, M., Ebel, A., Binkowski, F. S., and Shankar, U.:
530 Modal aerosol dynamics model for Europe, *Atmospheric Environment*, 32, 2981–2999,
531 [https://doi.org/10.1016/S1352-2310\(98\)00006-5](https://doi.org/10.1016/S1352-2310(98)00006-5), 1998.
- 532 Baldauf, M., Seifert, A., Förstner, J., Majewski, D., Raschendorfer, M., and Reinhardt, T.:
533 Operational Convective-Scale Numerical Weather Prediction with the COSMO Model:
534 Description and Sensitivities, *Mon. Wea. Rev.*, 139, 3887–3905,
535 <https://doi.org/10.1175/MWR-D-10-05013.1>, 2011.
- 536 Barker, D., Huang, X.-Y., Liu, Z., Auligné, T., Zhang, X., Rugg, S., Ajjaji, R., Bourgeois, A., Bray,
537 J., Chen, Y., Demirtas, M., Guo, Y.-R., Henderson, T., Huang, W., Lin, H.-C., Michalakes, J.,
538 Rizvi, S., and Zhang, X.: The Weather Research and Forecasting Model's Community
539 Variational/Ensemble Data Assimilation System: WRFDA, *Bull. Amer. Meteor. Soc.*, 93,
540 831–843, <https://doi.org/10.1175/BAMS-D-11-00167.1>, 2012.
- 541 Bauer, H.-S., Muppa, S. K., Wulfmeyer, V., Behrendt, A., Warrach-Sagi, K., and Späth, F.:
542 Multi-nested WRF simulations for studying planetary boundary layer processes on the
543 turbulence-permitting scale in a realistic mesoscale environment, *Tellus A: Dynamic
544 Meteorology and Oceanography*, 72, 1–28,
545 <https://doi.org/10.1080/16000870.2020.1761740>, 2020.
- 546 Bieser, J., Aulinger, A., Matthias, V., Quante, M., and van der Denier Gon, H. A. C.: Vertical
547 emission profiles for Europe based on plume rise calculations, *Environmental pollution
548 (Barking, Essex 1987)*, 159, 2935–2946, <https://doi.org/10.1016/j.envpol.2011.04.030>,
549 2011.
- 550 Bonavita, M., Hólm, E., Isaksen, I., and Fisher, M.: The evolution of the ECMWF hybrid data
551 assimilation system, *Q.J.R. Meteorol. Soc.*, 142, 287–303,
552 <https://doi.org/10.1002/qj.2652>, 2016.
- 553 Brasseur, G. P., Hauglustaine, D. A., Walters, S., Rasch, P. J., Müller, J.-F., Granier, C., and Tie,
554 X. X.: MOZART, a global chemical transport model for ozone and related chemical tracers:
555 1. Model description, *J. Geophys. Res.*, 103, 28265–28289,
556 <https://doi.org/10.1029/98JD02397>, 1998.
- 557 Butcher, G., Barnes, C., and Owen, L.: Landsat: The cornerstone of global land imaging, *GIM
558 International*, January/February 2019, 31–35, available at:
559 <http://pubs.er.usgs.gov/publication/70202363>, 2019.

560 Chan, P. W.: Determination of Richardson number profile from remote sensing data and its
561 aviation application, *IOP Conf. Ser.: Earth Environ. Sci.*, 1, 12043,
562 <https://doi.org/10.1088/1755-1315/1/1/012043>, 2008.

563 Chen, D., Liu, Z., Ban, J., Zhao, P., and Chen, M.: Retrospective analysis of 2015–2017
564 wintertime PM_{2.5} in China: response to emission regulations and the role of meteorology,
565 *Atmos. Chem. Phys.*, 19, 7409–7427, <https://doi.org/10.5194/acp-19-7409-2019>, 2019.

566 Copernicus: Copernicus official website, <https://atmosphere.copernicus.eu/>, last access: 21
567 July 2020.

568 Coppola, E., Sobolowski, S., Pichelli, E., Raffaele, F., Ahrens, B., Anders, I., Ban, N., Bastin, S.,
569 Belda, M., Belusic, D., Caldas-Alvarez, A., Cardoso, R. M., Davolio, S., Dobler, A.,
570 Fernandez, J., Fita, L., Fumiere, Q., Giorgi, F., Goergen, K., Güttler, I., Halenka, T.,
571 Heinzeller, D., Hodnebrog, Ø., Jacob, D., Kartsios, S., Katragkou, E., Kendon, E., Khodayar,
572 S., Kunstmann, H., Knist, S., Lavín-Gullón, A., Lind, P., Lorenz, T., Maraun, D., Marelle, L.,
573 van Meijgaard, E., Milovac, J., Myhre, G., Panitz, H.-J., Piazza, M., Raffa, M., Raub, T.,
574 Rockel, B., Schär, C., Sieck, K., Soares, P. M. M., Somot, S., Srnec, L., Stocchi, P., Tölle, M.
575 H., Truhetz, H., Vautard, R., Vries, H. de, and Warrach-Sagi, K.: A first-of-its-kind multi-
576 model convection permitting ensemble for investigating convective phenomena over
577 Europe and the Mediterranean, *Clim Dyn*, 55, 3–34, [https://doi.org/10.1007/s00382-018-](https://doi.org/10.1007/s00382-018-4521-8)
578 [4521-8](https://doi.org/10.1007/s00382-018-4521-8), 2020.

579 Corsmeier, U., Kalthoff, N., Barthlott, C., Aoshima, F., Behrendt, A., Di Girolamo, P.,
580 Dorninger, M., Handwerker, J., Kottmeier, C., Mahlke, H., Mobbs, S. D., Norton, E. G.,
581 Wickert, J., and Wulfmeyer, V.: Processes driving deep convection over complex terrain:
582 a multi-scale analysis of observations from COPS IOP 9c, *Q.J.R. Meteorol. Soc.*, 137, 137–
583 155, <https://doi.org/10.1002/qj.754>, 2011.

584 Danielson, J. J. and Gesch, D. B.: Global multi-resolution terrain elevation data 2010
585 (GMTED2010), Open-File report, 2011.

586 Denier van der Gon, H., Hendriks, C., Kuenen, J., Segers, A., and Visschedijk, A.: Description
587 of current temporal emission patterns and sensitivity of predicted AQ for temporal
588 emission patterns: EU FP7 MACC deliverable report D_D-EMIS_1.3, TNO report, 2011.

589 European Union: Copernicus Land Monitoring Service 2017, European Environment Agency,
590 2017.

591 European Union: Copernicus Land Monitoring Service 2012, European Environment Agency,
592 2012.

593 Fallmann, J.: Numerical simulations to assess the effect of urban heat island mitigation
594 strategies on regional air quality, PhD Thesis, Universität zu Köln, Cologne, 2014.

595 Fallmann, J., Forkel, R., and Emeis, S.: Secondary effects of urban heat island mitigation
596 measures on air quality, *Atmospheric Environment*, 125, 199–211,
597 <https://doi.org/10.1016/j.atmosenv.2015.10.094>, 2016.

598 Fallmann, J., Emeis, S., and Suppan, P.: Mitigation of urban heat stress – a modelling case
599 study for the area of Stuttgart, *DIE ERDE – Journal of the Geographical Society of Berlin*,
600 144, 202–216, <https://doi.org/10.12854/erde-144-15>, 2014.

601 Farr, T. G., Rosen, P. A., Caro, E., Crippen, R., Duren, R., Hensley, S., Kobrick, M., Paller, M.,
602 Rodriguez, E., Roth, L., Seal, D., Shaffer, S., Shimada, J., Umland, J., Werner, M., Oskin,

603 M., Burbank, D., and Alsdorf, D.: The Shuttle Radar Topography Mission, *Rev. Geophys.*,
604 45, <https://doi.org/10.1029/2005RG000183>, 2007.

605 Flemming, J., Huijnen, V., Arteta, J., Bechtold, P., Beljaars, A., Blechschmidt, A.-M.,
606 Diamantakis, M., Engelen, R. J., Gaudel, A., Inness, A., Jones, L., Josse, B., Katragkou, E.,
607 Marecal, V., Peuch, V.-H., Richter, A., Schultz, M. G., Stein, O., and Tsikerdekis, A.:
608 Tropospheric chemistry in the Integrated Forecasting System of ECMWF, *Geosci. Model*
609 *Dev.*, 8, 975–1003, <https://doi.org/10.5194/gmd-8-975-2015>, 2015.

610 Forkel, R., Balzarini, A., Baró, R., Bianconi, R., Curci, G., Jiménez-Guerrero, P., Hirtl, M.,
611 Honzak, L., Lorenz, C., Im, U., Pérez, J. L., Pirovano, G., San José, R., Tuccella, P., Werhahn,
612 J., and Žabkar, R.: Analysis of the WRF-Chem contributions to AQMEII phase2 with
613 respect to aerosol radiative feedbacks on meteorology and pollutant distributions,
614 *Atmospheric Environment*, 115, 630–645,
615 <https://doi.org/10.1016/j.atmosenv.2014.10.056>, 2015.

616 Freitas, S. R., Longo, K. M., Alonso, M. F., Pirre, M., Marecal, V., Grell, G., Stockler, R., Mello,
617 R. F., and Sánchez Gácita, M.: PREP-CHEM-SRC – 1.0: a preprocessor of trace gas and
618 aerosol emission fields for regional and global atmospheric chemistry models, *Geosci.*
619 *Model Dev.*, 4, 419–433, <https://doi.org/10.5194/gmd-4-419-2011>, 2011.

620 Freitas, S. R., Panetta, J., Longo, K. M., Rodrigues, L. F., Moreira, D. S., Rosário, N. E., Silva
621 Dias, P. L., Silva Dias, M. A. F., Souza, E. P., Freitas, E. D., Longo, M., Frassoni, A., Fazenda,
622 A. L., Santos e Silva, C. M., Pavani, C. A. B., Eiras, D., França, D. A., Massaru, D., Silva, F. B.,
623 Santos, F. C., Pereira, G., Camponogara, G., Ferrada, G. A., Campos Velho, H. F., Menezes,
624 I., Freire, J. L., Alonso, M. F., Gácita, M. S., Zazur, M., Fonseca, R. M., Lima, R. S., Siqueira,
625 R. A., Braz, R., Tomita, S., Oliveira, V., and Martins, L. D.: The Brazilian developments on
626 the Regional Atmospheric Modeling System (BRAMS 5.2): an integrated environmental
627 model tuned for tropical areas, *Geosci. Model Dev.*, 10, 189–222,
628 <https://doi.org/10.5194/gmd-10-189-2017>, 2017.

629 García-Díez, M., Lauwaet, D., Hooyberghs, H., Ballester, J., Ridder, K. de, and Rodó, X.:
630 Advantages of using a fast urban boundary layer model as compared to a full mesoscale
631 model to simulate the urban heat island of Barcelona, *Geosci. Model Dev.*, 9, 4439–4450,
632 <https://doi.org/10.5194/gmd-9-4439-2016>, 2016.

633 Giorgi, F., Coppola, E., Solmon, F., Mariotti, L., Sylla, M. B., Bi, X., Elguindi, N., Diro, G. T.,
634 Nair, V., Giuliani, G., Turuncoglu, U. U., Cozzini, S., Güttler, I., O’Brien, T. A., Tawfik, A. B.,
635 Shalaby, A., Zakey, A. S., Steiner, A. L., Stordal, F., Sloan, L. C., and Brankovic, C.: RegCM4:
636 model description and preliminary tests over multiple CORDEX domains, *Clim. Res.*, 52,
637 7–29, <https://doi.org/10.3354/cr01018>, 2012.

638 Granier, C., Darras, S., Denier van der Gon, H., Doubalova, J., Elguindi, N., Galle, B., Gauss,
639 M., Guevara, M., Jalkanen, J.-P., Kuenen, J., Liousse, C., Quack, B., Simpson, D., and
640 Sindelarova, K.: The Copernicus Atmosphere Monitoring Service global and regional
641 emissions (April 2019 version), 2019.

642 Grell, G. A., Peckham, S. E., Schmitz, R., McKeen, S. A., Frost, G., Skamarock, W. C., and Eder,
643 B.: Fully coupled “online” chemistry within the WRF model, *Atmospheric Environment*,
644 39, 6957–6975, <https://doi.org/10.1016/j.atmosenv.2005.04.027>, 2005.

645 Guevara, M., Jorba, O., Tena, C., van der Denier Gon, H., Kuenen, J., Elguindi-Solmon, N.,
646 Darras, S., Granier, C., and Pérez García-Pando, C.: CAMS-TEMPO: global and European
647 emission temporal profile maps for atmospheric chemistry modelling, 2020.

648 Heinze, R., Moseley, C., Böske, L. N., Muppa, S. K., Maurer, V., Raasch, S., and Stevens, B.:
649 Evaluation of large-eddy simulations forced with mesoscale model output for a multi-
650 week period during a measurement campaign, *Atmos. Chem. Phys.*, 17, 7083–7109,
651 <https://doi.org/10.5194/acp-17-7083-2017>, 2017a.

652 Heinze, R., Dipankar, A., Henken, C. C., Moseley, C., Sourdeval, O., Trömel, S., Xie, X.,
653 Adamidis, P., Ament, F., Baars, H., Barthlott, C., Behrendt, A., Blahak, U., Bley, S., Brdar,
654 S., Brueck, M., Crewell, S., Deneke, H., Di Girolamo, P., Evaristo, R., Fischer, J., Frank, C.,
655 Friederichs, P., Göcke, T., Gorges, K., Hande, L., Hanke, M., Hansen, A., Hege, H.-C.,
656 Hoose, C., Jahns, T., Kalthoff, N., Klocke, D., Kneifel, S., Knippertz, P., Kuhn, A., van Laar,
657 T., Macke, A., Maurer, V., Mayer, B., Meyer, C. I., Muppa, S. K., Neggers, R. A. J., Orlandi,
658 E., Pantillon, F., Pospichal, B., Röber, N., Scheck, L., Seifert, A., Seifert, P., Senf, F., Siligam,
659 P., Simmer, C., Steinke, S., Stevens, B., Wapler, K., Weniger, M., Wulfmeyer, V., Zängl, G.,
660 Zhang, D., and Quaas, J.: Large-eddy simulations over Germany using ICON: a
661 comprehensive evaluation, *Q.J.R. Meteorol. Soc.*, 143, 69–100,
662 <https://doi.org/10.1002/qj.2947>, 2017b.

663 Hengl, T., Heuvelink, G. B. M., Kempen, B., Leenaars, J. G. B., Walsh, M. G., Shepherd, K. D.,
664 Sila, A., MacMillan, R. A., Mendes de Jesus, J., Tamene, L., and Tondoh, J. E.: Mapping Soil
665 Properties of Africa at 250 m Resolution: Random Forests Significantly Improve Current
666 Predictions, *PloS one*, 10, e0125814, <https://doi.org/10.1371/journal.pone.0125814>,
667 2015.

668 Hengl, T., Jesus, J. M. de, MacMillan, R. A., Batjes, N. H., Heuvelink, G. B. M., Ribeiro, E.,
669 Samuel-Rosa, A., Kempen, B., Leenaars, J. G. B., Walsh, M. G., and Gonzalez, M. R.:
670 SoilGrids1km--global soil information based on automated mapping, *PloS one*, 9,
671 e105992, <https://doi.org/10.1371/journal.pone.0105992>, 2014.

672 Hong, S.-Y., Noh, Y., and Dudhia, J.: A New Vertical Diffusion Package with an Explicit
673 Treatment of Entrainment Processes, *Mon. Wea. Rev.*, 134, 2318–2341,
674 <https://doi.org/10.1175/MWR3199.1>, 2006.

675 Honnert, R. and Masson, V.: What is the smallest physically acceptable scale for 1D
676 turbulence schemes?, *Front. Earth Sci.*, 2, 27, <https://doi.org/10.3389/feart.2014.00027>,
677 2014.

678 Honnert, R., Efstathiou, G. A., Beare, R. J., Ito, J., Lock, A., Neggers, R., Plant, R. S., Shin, H. H.,
679 Tomassini, L., and Zhou, B.: The Atmospheric Boundary Layer and the “Gray Zone” of
680 Turbulence: A Critical Review, *J. Geophys. Res. Atmos.*, 125,
681 <https://doi.org/10.1029/2019JD030317>, 2020.

682 Horowitz, L. W., Walters, S., Mauzerall, D. L., Emmons, L. K., Rasch, P. J., Granier, C., Tie, X.,
683 Lamarque, J.-F., Schultz, M. G., Tyndall, G. S., Orlando, J. J., and Brasseur, G. P.: A global
684 simulation of tropospheric ozone and related tracers: Description and evaluation of
685 MOZART, version 2, *J. Geophys. Res.*, 108, n/a-n/a,
686 <https://doi.org/10.1029/2002JD002853>, 2003.

687 Huszar, P., Karlický, J., Ďoubalová, J., Šindelářová, K., Nováková, T., Belda, M., Halenka, T.,
688 Žák, M., and Pišoft, P.: Urban canopy meteorological forcing and its impact on ozone and

689 PM_{2.5}: role of vertical turbulent transport, *Atmos. Chem. Phys.*, 20, 1977–2016,
690 <https://doi.org/10.5194/acp-20-1977-2020>, 2020.

691 Iacono, M. J., Delamere, J. S., Mlawer, E. J., Shephard, M. W., Clough, S. A., and Collins, W.
692 D.: Radiative forcing by long-lived greenhouse gases: Calculations with the AER radiative
693 transfer models, *J. Geophys. Res.*, 113, <https://doi.org/10.1029/2008JD009944>, 2008.

694 Inness, A., Ades, M., Agustí-Panareda, A., Barré, J., Benedictow, A., Blechschmidt, A.-M.,
695 Dominguez, J. J., Engelen, R., Eskes, H., Flemming, J., Huijnen, V., Jones, L., Kipling, Z.,
696 Massart, S., Parrington, M., Peuch, V.-H., Razinger, M., Remy, S., Schulz, M., and Suttie,
697 M.: The CAMS reanalysis of atmospheric composition, *Atmos. Chem. Phys.*, 19, 3515–
698 3556, <https://doi.org/10.5194/acp-19-3515-2019>, 2019.

699 Jiménez, P. A., Dudhia, J., González-Rouco, J. F., Navarro, J., Montávez, J. P., and García-
700 Bustamante, E.: A Revised Scheme for the WRF Surface Layer Formulation, *Mon. Wea.*
701 *Rev.*, 140, 898–918, <https://doi.org/10.1175/MWR-D-11-00056.1>, 2012.

702 Jin, L., Li, Z., He, Q., Miao, Q., Zhang, H., and Yang, X.: Observation and simulation of near-
703 surface wind and its variation with topography in Urumqi, West China, *J Meteorol Res*,
704 30, 961–982, <https://doi.org/10.1007/s13351-016-6012-3>, 2016.

705 Karlický, J., Huszár, P., Nováková, T., Belda, M., Švábik, F., Ďoubalová, J., and Halenka, T.: The
706 'urban meteorology island': a multi-model ensemble analysis, 2020.

707 Kawabata, T., Schwitalla, T., Adachi, A., Bauer, H.-S., Wulfmeyer, V., Nagumo, N., and
708 Yamauchi, H.: Observational operators for dual polarimetric radars in variational data
709 assimilation systems (PolRad VAR v1.0), *Geosci. Model Dev.*, 11, 2493–2501,
710 <https://doi.org/10.5194/gmd-11-2493-2018>, 2018.

711 Kealy, J. C., Efstathiou, G. A., and Beare, R. J.: The Onset of Resolved Boundary-Layer
712 Turbulence at Grey-Zone Resolutions, *Boundary-Layer Meteorol*, 171, 31–52,
713 <https://doi.org/10.1007/s10546-018-0420-0>, 2019.

714 Khan, B., Banzhaf, S., Chan, E. C., Forkel, R., Kanani-Sühring, F., Ketelsen, K., Kurppa, M.,
715 Maronga, B., Mauder, M., Raasch, S., Russo, E., Schaap, M., and Sühring, M.:
716 Development of an atmospheric chemistry model coupled to the PALM model system
717 6.0: Implementation and first applications, *Geosci. Model Dev.*,
718 <https://doi.org/10.5194/gmd-2020-286>, 2020.

719 Kosovic, B.: Subgrid-scale modelling for the large-eddy simulation of high-Reynolds-number
720 boundary layers, *J. Fluid Mech.*, 336, 151–182,
721 <https://doi.org/10.1017/S0022112096004697>, 1997.

722 Kuenen, J. J. P., Visschedijk, A. J. H., Jozwicka, M., and van der Denier Gon, H. A. C.: TNO-
723 MACC-II emission inventory; a multi-year (2003–2009) consistent high-resolution
724 European emission inventory for air quality modelling, *Atmos. Chem. Phys.*, 14, 10963–
725 10976, <https://doi.org/10.5194/acp-14-10963-2014>, 2014.

726 Kuik, F., Kerschbaumer, A., Lauer, A., Lupascu, A., Schneidemesser, E. von, and Butler, T. M.:
727 Top-down quantification of NO_x emissions from traffic in an urban area using a high-
728 resolution regional atmospheric chemistry model, *Atmos. Chem. Phys.*, 18, 8203–8225,
729 <https://doi.org/10.5194/acp-18-8203-2018>, 2018.

730 Kuik, F., Lauer, A., Churkina, G., van der Denier Gon, H. A. C., Fenner, D., Mar, K. A., and
731 Butler, T. M.: Air quality modelling in the Berlin–Brandenburg region using WRF-Chem

732 v3.7.1: sensitivity to resolution of model grid and input data, *Geosci. Model Dev.*, 9,
733 4339–4363, <https://doi.org/10.5194/gmd-9-4339-2016>, 2016.

734 Kusaka, H. and Kimura, F.: Coupling a Single-Layer Urban Canopy Model with a Simple
735 Atmospheric Model: Impact on Urban Heat Island Simulation for an Idealized Case, *JMSJ*,
736 82, 67–80, <https://doi.org/10.2151/jmsj.82.67>, 2004.

737 Lee, T. R. and Wekker, S. F. J. de: Estimating Daytime Planetary Boundary Layer Heights over
738 a Valley from Rawinsonde Observations at a Nearby Airport: An Application to the Page
739 Valley in Virginia, United States, *J. Appl. Meteor. Climatol.*, 55, 791–809,
740 <https://doi.org/10.1175/JAMC-D-15-0300.1>, 2016.

741 Li, Z., Zhou, Y., Wan, B., Chung, H., Huang, B., and Liu, B.: Model evaluation of high-
742 resolution urban climate simulations: using the WRF/Noah LSM/SLUCM model (Version
743 3.7.1) as a case study, *Geosci. Model Dev.*, 12, 4571–4584, <https://doi.org/10.5194/gmd-12-4571-2019>, 2019.

745 Lin, D., Khan, B., Katurji, M., Bird, L., Faria, R., and Revell, L. E.: WRF4PALM v1.0: A Mesoscale
746 Dynamical Driver for the Microscale PALM Model System 6.0, 2020.

747 Mailler, S., Menut, L., Khvorostyanov, D., Valari, M., Couvidat, F., Siour, G., Turquety, S.,
748 Briant, R., Tuccella, P., Bessagnet, B., Colette, A., Létinois, L., Markakis, K., and Meleux, F.:
749 CHIMERE-2017: from urban to hemispheric chemistry-transport modeling, *Geosci. Model*
750 *Dev.*, 10, 2397–2423, <https://doi.org/10.5194/gmd-10-2397-2017>, 2017.

751 Manders, A. M. M., Builtjes, P. J. H., Curier, L., van der Denier Gon, H. A. C., Hendriks, C.,
752 Jonkers, S., Kranenburg, R., Kuenen, J. J. P., Segers, A. J., Timmermans, R. M. A.,
753 Visschedijk, A. J. H., Wichink Kruit, R. J., van Pul, W. A. J., Sauter, F. J., van der Swaluw, E.,
754 Swart, D. P. J., Douros, J., Eskes, H., van Meijgaard, E., van Ulft, B., van Velthoven, P.,
755 Banzhaf, S., Mues, A. C., Stern, R., Fu, G., Lu, S., Heemink, A., van Velzen, N., and Schaap,
756 M.: Curriculum vitae of the LOTOS–EUROS (v2.0) chemistry transport model, *Geosci.*
757 *Model Dev.*, 10, 4145–4173, <https://doi.org/10.5194/gmd-10-4145-2017>, 2017.

758 Mar, K. A., Ojha, N., Pozzer, A., and Butler, T. M.: Ozone air quality simulations with WRF-
759 Chem (v3.5.1) over Europe: model evaluation and chemical mechanism comparison,
760 *Geosci. Model Dev.*, 9, 3699–3728, <https://doi.org/10.5194/gmd-9-3699-2016>, 2016.

761 Marécal, V., Peuch, V.-H., Andersson, C., Andersson, S., Arteta, J., Beekmann, M.,
762 Benedictow, A., Bergström, R., Bessagnet, B., Cansado, A., Chérour, F., Colette, A.,
763 Coman, A., Curier, R. L., van der Denier Gon, H. A. C., Drouin, A., Elbern, H., Emili, E.,
764 Engelen, R. J., Eskes, H. J., Foret, G., Friese, E., Gauss, M., Giannaros, C., Guth, J., Joly, M.,
765 Jaumouillé, E., Josse, B., Kadygrov, N., Kaiser, J. W., Krajsek, K., Kuenen, J., Kumar, U.,
766 Liora, N., Lopez, E., Malherbe, L., Martinez, I., Melas, D., Meleux, F., Menut, L., Moinat,
767 P., Morales, T., Parmentier, J., Piacentini, A., Plu, M., Poupkou, A., Queguiner, S.,
768 Robertson, L., Rouil, L., Schaap, M., Segers, A., Sofiev, M., Tarasson, L., Thomas, M.,
769 Timmermans, R., Valdebenito, Á., van Velthoven, P., van Versendaal, R., Vira, J., and Ung,
770 A.: A regional air quality forecasting system over Europe: the MACC-II daily ensemble
771 production, *Geosci. Model Dev.*, 8, 2777–2813, <https://doi.org/10.5194/gmd-8-2777-2015>, 2015.

773 Maronga, B., Gryscha, M., Heinze, R., Hoffmann, F., Kanani-Sühring, F., Keck, M., Ketelsen,
774 K., Letzel, M. O., Sühring, M., and Raasch, S.: The Parallelized Large-Eddy Simulation
775 Model (PALM) version 4.0 for atmospheric and oceanic flows: model formulation, recent

776 developments, and future perspectives, *Geosci. Model Dev.*, 8, 2515–2551,
777 <https://doi.org/10.5194/gmd-8-2515-2015>, 2015.

778 Maronga, B., Banzhaf, S., Burmeister, C., Esch, T., Forkel, R., Fröhlich, D., Fuka, V., Gehrke, K.
779 F., Geletič, J., Giersch, S., Gronemeier, T., Groß, G., Heldens, W., Hellsten, A., Hoffmann,
780 F., Inagaki, A., Kadasch, E., Kanani-Sühring, F., Ketelsen, K., Khan, B. A., Knigge, C., Knoop,
781 H., Krč, P., Kurppa, M., Maamari, H., Matzarakis, A., Mauder, M., Pallasch, M., Pavlik, D.,
782 Pfafferott, J., Resler, J., Rissmann, S., Russo, E., Salim, M., Schrempf, M., Schwenkel, J.,
783 Seckmeyer, G., Schubert, S., Sühring, M., Tils, R. von, Vollmer, L., Ward, S., Witha, B.,
784 Wurps, H., Zeidler, J., and Raasch, S.: Overview of the PALM model system 6.0, *Geosci.*
785 *Model Dev.*, 13, 1335–1372, <https://doi.org/10.5194/gmd-13-1335-2020>, 2020.

786 Maronga, B., Gross, G., Raasch, S., Banzhaf, S., Forkel, R., Heldens, W., Kanani-Sühring, F.,
787 Matzarakis, A., Mauder, M., Pavlik, D., Pfafferott, J., Schubert, S., Seckmeyer, G., Sieker,
788 H., and Winderlich, K.: Development of a new urban climate model based on the model
789 PALM – Project overview, planned work, and first achievements, *metz*, 28, 105–119,
790 <https://doi.org/10.1127/metz/2019/0909>, 2019.

791 Marsh, D. R., Mills, M. J., Kinnison, D. E., Lamarque, J.-F., Calvo, N., and Polvani, L. M.:
792 Climate Change from 1850 to 2005 Simulated in CESM1(WACCM), *J. Climate*, 26, 7372–
793 7391, <https://doi.org/10.1175/JCLI-D-12-00558.1>, 2013.

794 Martilli, A., Clappier, A., and Rotach, M. W.: An Urban Surface Exchange Parameterisation for
795 Mesoscale Models, *Boundary-Layer Meteorology*, 104, 261–304,
796 <https://doi.org/10.1023/A:1016099921195>, 2002.

797 Memmesheimer, M., Friese, E., Ebel, A., Jakobs, H. J., Feldmann, H., Kessler, C., and Piekorz,
798 G.: Long-term simulations of particulate matter in Europe on different scales using
799 sequential nesting of a regional model, *IJEP*, 22, 108,
800 <https://doi.org/10.1504/IJEP.2004.005530>, 2004.

801 Nakayama, H., Takemi, T., and Nagai, H.: Large-eddy simulation of urban boundary-layer
802 flows by generating turbulent inflows from mesoscale meteorological simulations,
803 *Atmosph. Sci. Lett.*, 13, 180–186, <https://doi.org/10.1002/asl.377>, 2012.

804 Niu, G.-Y., Yang, Z.-L., Mitchell, K. E., Chen, F., Ek, M. B., Barlage, M., Kumar, A., Manning, K.,
805 Niyogi, D., Rosero, E., Tewari, M., and Xia, Y.: The community Noah land surface model
806 with multiparameterization options (Noah-MP): 1. Model description and evaluation with
807 local-scale measurements, *J. Geophys. Res.*, 116, <https://doi.org/10.1029/2010JD015139>,
808 2011.

809 Panosetti, D., Böing, S., Schlemmer, L., and Schmidli, J.: Idealized Large-Eddy and Convection-
810 Resolving Simulations of Moist Convection over Mountainous Terrain, *J. Atmos. Sci.*, 73,
811 4021–4041, <https://doi.org/10.1175/JAS-D-15-0341.1>, 2016.

812 Pfister, G. G., Parrish, D. D., Worden, H., Emmons, L. K., Edwards, D. P., Wiedinmyer, C.,
813 Diskin, G. S., Huey, G., Oltmans, S. J., Thouret, V., Weinheimer, A., and Wisthaler, A.:
814 Characterizing summertime chemical boundary conditions for airmasses entering the US
815 West Coast, *Atmos. Chem. Phys.*, 11, 1769–1790, [https://doi.org/10.5194/acp-11-1769-](https://doi.org/10.5194/acp-11-1769-2011)
816 2011, 2011.

817 Prein, A. F., Langhans, W., Fosser, G., Ferrone, A., Ban, N., Goergen, K., Keller, M., Tölle, M.,
818 Gutjahr, O., Feser, F., Brisson, E., Kollet, S., Schmidli, J., van Lipzig, N. P. M., and Leung, R.:
819 A review on regional convection-permitting climate modeling: Demonstrations,

820 prospects, and challenges, *Rev. Geophys.*, 53, 323–361,
821 <https://doi.org/10.1002/2014RG000475>, 2015.

822 Resler, J., Eben, K., Geletič, J., Krč, P., Rosecký, M., Sühning, M., Belda, M., Fuka, V., Halenka,
823 T., Huszár, P., Karlický, J., Benešová, N., Ďoubalová, J., Honzáková, K., Keder, J.,
824 Nápravníková, Š., and Vlček, O.: Validation of the PALM model system 6.0 in real urban
825 environment; case study of Prague-Dejvice, Czech Republic, *Geosci. Model Dev.*,
826 <https://doi.org/10.5194/gmd-2020-175>, 2020, under review.

827 Rieger, D., Bangert, M., Bischoff-Gauss, I., Förstner, J., Lundgren, K., Reinert, D., Schröter, J.,
828 Vogel, H., Zängl, G., Ruhnke, R., and Vogel, B.: ICON–ART 1.0 – a new online-coupled
829 model system from the global to regional scale, *Geosci. Model Dev.*, 8, 1659–1676,
830 <https://doi.org/10.5194/gmd-8-1659-2015>, 2015.

831 Salamanca, F. and Martilli, A.: A new Building Energy Model coupled with an Urban Canopy
832 Parameterization for urban climate simulations—part II. Validation with one dimension
833 off-line simulations, *Theor Appl Climatol*, 99, 345–356, [https://doi.org/10.1007/s00704-](https://doi.org/10.1007/s00704-009-0143-8)
834 [009-0143-8](https://doi.org/10.1007/s00704-009-0143-8), 2010.

835 Schell, B., Ackermann, I. J., Hass, H., Binkowski, F. S., and Ebel, A.: Modeling the formation of
836 secondary organic aerosol within a comprehensive air quality model system, *J. Geophys.*
837 *Res.*, 106, 28275–28293, <https://doi.org/10.1029/2001JD000384>, 2001.

838 Scherer, D., Antretter, F., Bender, S., Cortekar, J., Emeis, S., Fehrenbach, U., Gross, G., Halbig,
839 G., Hasse, J., Maronga, B., Raasch, S., and Scherber, K.: Urban Climate Under Change
840 [UC]2 – A National Research Programme for Developing a Building-Resolving
841 Atmospheric Model for Entire City Regions, *metz*, 28, 95–104,
842 <https://doi.org/10.1127/metz/2019/0913>, 2019.

843 Schwitalla, T.: Simulation of NO₂ concentration over the Stuttgart metropolitan area, TIB AV-
844 Portal, <https://doi.org/10.5446/50923>, 2021a.

845 Schwitalla, T.: Simulation of PM₁₀ concentration over the Stuttgart metropolitan area, TIB
846 AV-Portal, <https://doi.org/10.5446/50924>, 2021b.

847 Seidel, D. J., Zhang, Y., Beljaars, A., Golaz, J.-C., Jacobson, A. R., and Medeiros, B.:
848 Climatology of the planetary boundary layer over the continental United States and
849 Europe, *J. Geophys. Res.*, 117, n/a-n/a, <https://doi.org/10.1029/2012JD018143>, 2012.

850 Skamarock, W. C., Klemp, J. B., Dudhia, J., Gill, D. O., Liu, Z., Berner, J., Wang, W., Powers, J.
851 G., Duda, M. G., Barker, D. M., and Huang, X.-Y.: A Description of the Advanced Research
852 WRF Model Version 4, 2019.

853 Steeneveld, G. J., Ronda, R. J., and Holtslag, A. A. M.: The Challenge of Forecasting the Onset
854 and Development of Radiation Fog Using Mesoscale Atmospheric Models, *Boundary-*
855 *Layer Meteorol*, 154, 265–289, <https://doi.org/10.1007/s10546-014-9973-8>, 2015.

856 Stockwell, W. R., Middleton, P., Chang, J. S., and Tang, X.: The second generation regional
857 acid deposition model chemical mechanism for regional air quality modeling, *J. Geophys.*
858 *Res.*, 95, 16343, <https://doi.org/10.1029/JD095iD10p16343>, 1990.

859 Stuttgart Municipality and German Meteorological Service (DWD): Requirements for fine
860 dust situations, <https://feinstaubalarm.stuttgart.de/img/mdb/item/584405/119353.pdf>,
861 last access: 20 August 2020, 2019.

862 Sun, W., Liu, Z., Chen, D., Zhao, P., and Chen, M.: Development and application of the
863 WRFDA-Chem three-dimensional variational (3DVAR) system: aiming to improve air

864 quality forecasting and diagnose model deficiencies, *Atmos. Chem. Phys.*, 20, 9311–9329,
865 <https://doi.org/10.5194/acp-20-9311-2020>, 2020.

866 Teixeira, J. C., Fallmann, J., Carvalho, A. C., and Rocha, A.: Surface to boundary layer coupling
867 in the urban area of Lisbon comparing different urban canopy models in WRF, *Urban*
868 *Climate*, 28, 100454, <https://doi.org/10.1016/j.uclim.2019.100454>, 2019.

869 Thompson, G., Field, P. R., Rasmussen, R. M., and Hall, W. D.: Explicit Forecasts of Winter
870 Precipitation Using an Improved Bulk Microphysics Scheme. Part II: Implementation of a
871 New Snow Parameterization, *Mon. Wea. Rev.*, 136, 5095–5115,
872 <https://doi.org/10.1175/2008MWR2387.1>, 2008.

873 Thundathil, R., Schwitalla, T., Behrendt, A., Muppa, S. K., ADAM, S., and Wulfmeyer, V.:
874 Assimilation of Lidar Water Vapour Mixing Ratio and Temperature Profiles into a
875 Convection-Permitting Model, *JMSJ*, <https://doi.org/10.2151/jmsj.2020-049>, 2020.

876 Thunis, P., Degraeuwe, B., Pisoni, E., Trombetti, M., Peduzzi, E., Belis, C. A., Wilson, J., and
877 Vignati, E.: Urban PM_{2.5} atlas: Air quality in European cities, JRC science for policy report,
878 28804, Publications Office, Luxembourg, 1 online resource, 2017.

879 UN: The World's Cities in 2018, United Nations, 2018.

880 Valcke, S., Balaji, V., Craig, A., DeLuca, C., Dunlap, R., Ford, R. W., Jacob, R., Larson, J.,
881 O'Kuinghttons, R., Riley, G. D., and Vertenstein, M.: Coupling technologies for Earth
882 System Modelling, *Geosci. Model Dev.*, 5, 1589–1596, [https://doi.org/10.5194/gmd-5-](https://doi.org/10.5194/gmd-5-1589-2012)
883 [1589-2012](https://doi.org/10.5194/gmd-5-1589-2012), 2012.

884 Vogel, B., Vogel, H., Bäumer, D., Bangert, M., Lundgren, K., Rinke, R., and Stanelle, T.: The
885 comprehensive model system COSMO-ART – Radiative impact of aerosol on the state of
886 the atmosphere on the regional scale, *Atmos. Chem. Phys.*, 9, 8661–8680,
887 <https://doi.org/10.5194/acp-9-8661-2009>, 2009.

888 Wang, D., Stachlewska, I. S., Song, X., Heese, B., and Nemuc, A.: Variability of the Boundary
889 Layer Over an Urban Continental Site Based on 10 Years of Active Remote Sensing
890 Observations in Warsaw, *Remote Sensing*, 12, 340, <https://doi.org/10.3390/rs12020340>,
891 2020.

892 WHO: WHO Air quality guidelines for particulate matter, ozone, nitrogen dioxide and sulfur
893 dioxide. Global update 2005., 2005.

894 Yang, Z.-L., Niu, G.-Y., Mitchell, K. E., Chen, F., Ek, M. B., Barlage, M., Longuevergne, L.,
895 Manning, K., Niyogi, D., Tewari, M., and Xia, Y.: The community Noah land surface model
896 with multiparameterization options (Noah-MP): 2. Evaluation over global river basins, *J.*
897 *Geophys. Res.*, 116, <https://doi.org/10.1029/2010JD015140>, 2011.

898 Zängl, G., Reinert, D., Rípodas, P., and Baldauf, M.: The ICON (ICOsahedral Non-hydrostatic)
899 modelling framework of DWD and MPI-M: Description of the non-hydrostatic dynamical
900 core, *Q.J.R. Meteorol. Soc.*, 141, 563–579, <https://doi.org/10.1002/qj.2378>, 2015.

901 Zhang, X., Huang, X.-Y., Liu, J., Poterjoy, J., Weng, Y., Zhang, F., and Wang, H.: Development
902 of an Efficient Regional Four-Dimensional Variational Data Assimilation System for WRF,
903 *Journal of Atmospheric and Oceanic Technology*, 31, 2777–2794,
904 <https://doi.org/10.1175/JTECH-D-13-00076.1>, 2014.

905 Zhong, M., Saikawa, E., Liu, Y., Naik, V., Horowitz, L. W., Takigawa, M., Zhao, Y., Lin, N.-H.,
906 and Stone, E. A.: Air quality modeling with WRF-Chem v3.5 in East Asia: sensitivity to

907 emissions and evaluation of simulated air quality, *Geosci. Model Dev.*, 9, 1201–1218,
908 <https://doi.org/10.5194/gmd-9-1201-2016>, 2016.

909 Zieliński, M., Fortuniak, K., Pawlak, W., and Siedlecki, M.: Long-term Turbulent Sensible-
910 Heat-Flux Measurements with a Large-Aperture Scintillometer in the Centre of Łódź,
911 Central Poland, *Boundary-Layer Meteorol.*, 167, 469–492,
912 <https://doi.org/10.1007/s10546-017-0331-5>, 2018.

913

914

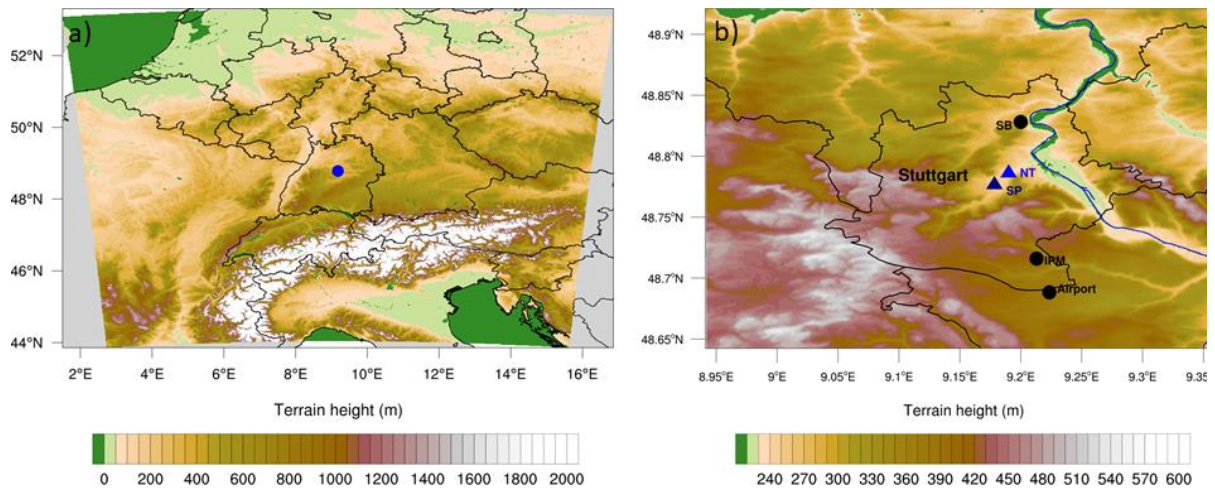


Figure 1: Model domain 1 (a) and domain 3 (b). The blue dot in (a) denotes Stuttgart. Black dots in (b) show the location of the meteorological measurement sites. The diamonds in (b) denotes the Neckartor (NT) and Schlossplatz (SP) locations and the blue contour line denotes the Neckar River (River data © OpenStreetMap contributors 2020. Distributed under a Creative Commons BY-SA License).

915

916

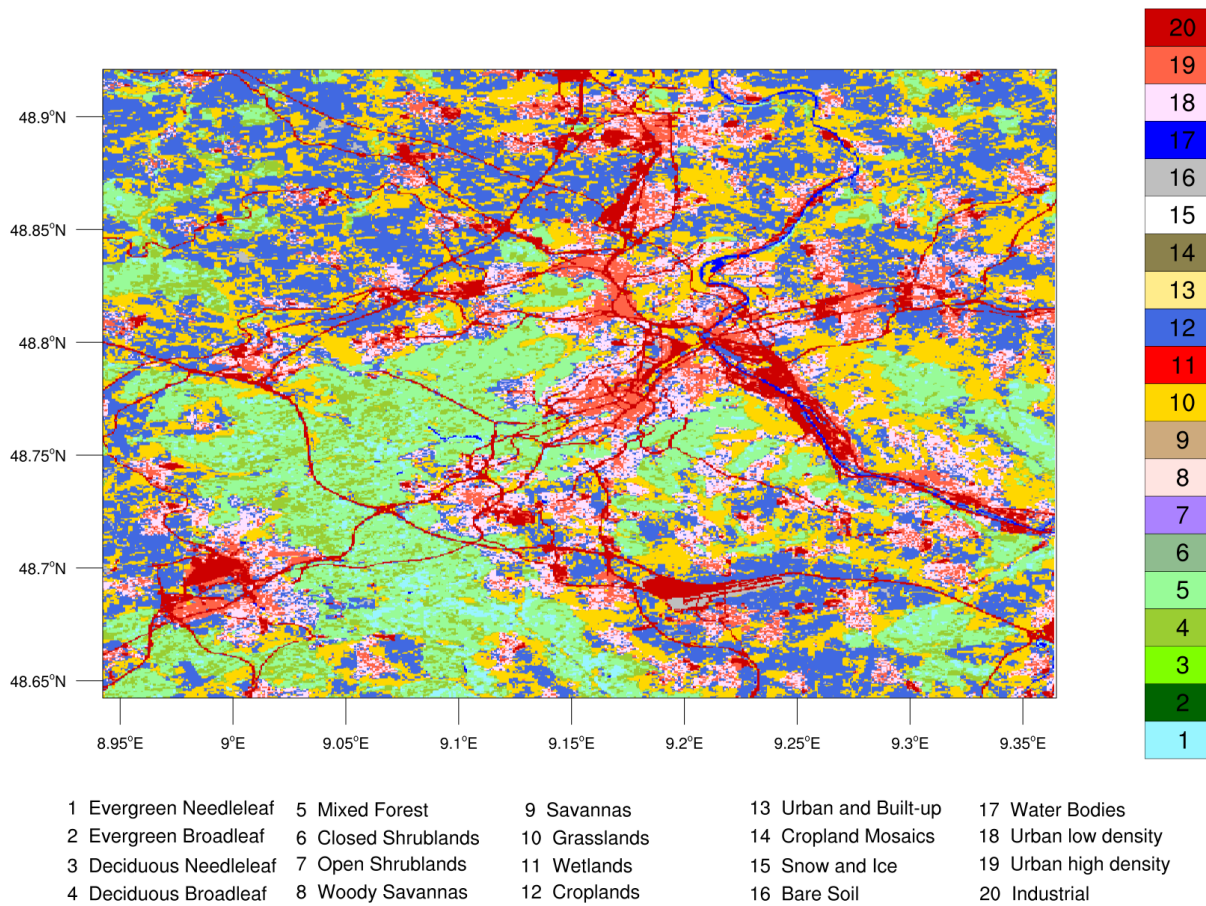


Figure 2: Land cover data from the Baden-Württemberg State Institute for the Environment (LUBW) reclassified for WRF in the innermost domain at a resolution of 50 m.

917

918

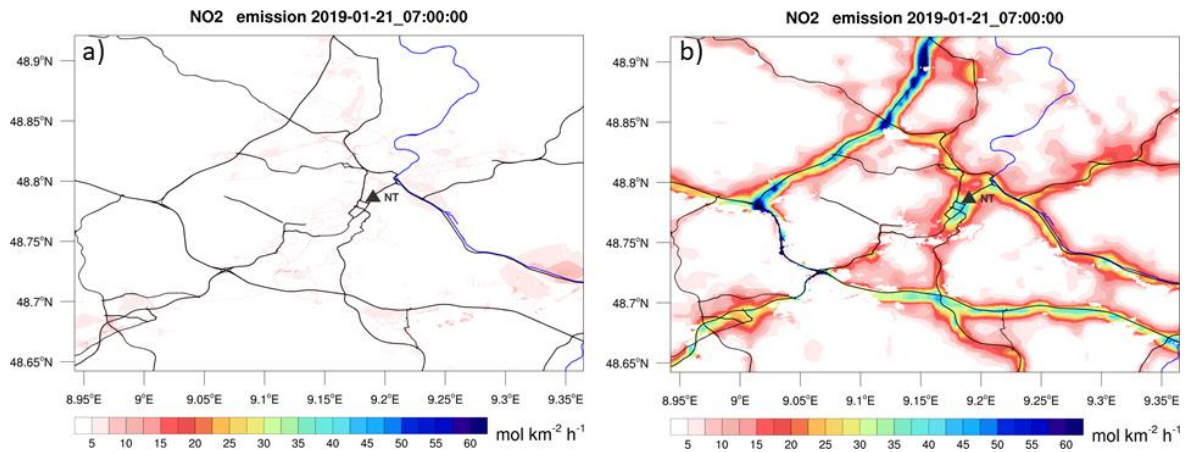


Figure 3: NO₂ emissions valid at 07 UTC on January 21, 2019. (a) shows the emissions derived from the CAMS-REG-AP data set and (b) shows the emissions derived from the BW-EMISS data set (Map Data © OpenStreetMap contributors 2020. Distributed under a Creative Commons BY-SA License).

919

920

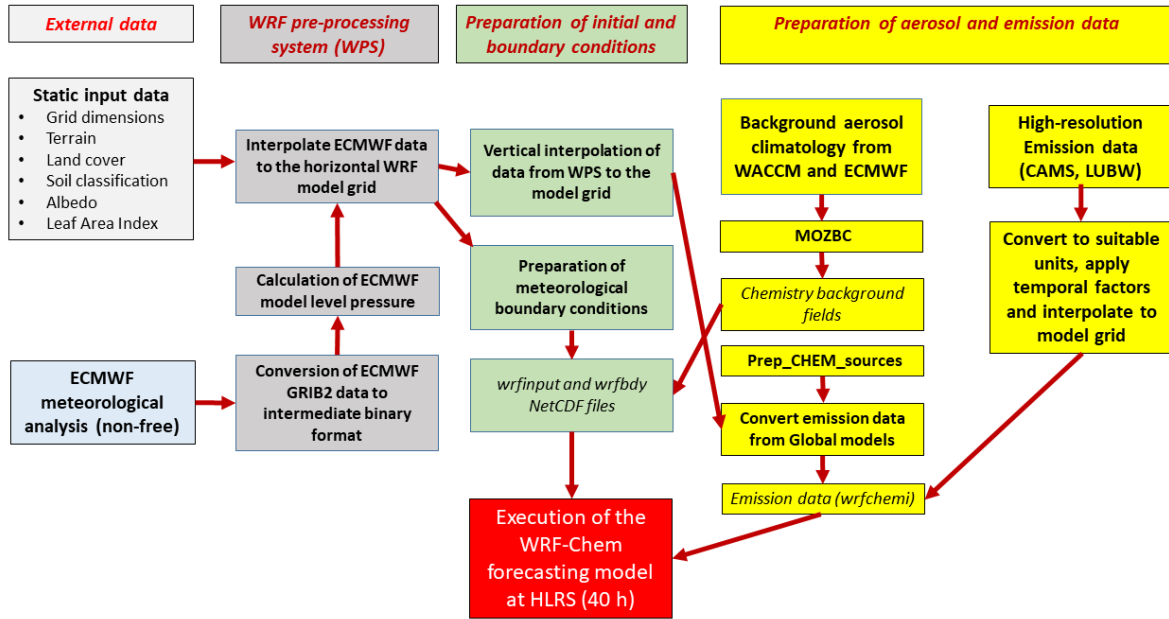


Figure 4: Workflow of the AQFS prototype system.

921

922

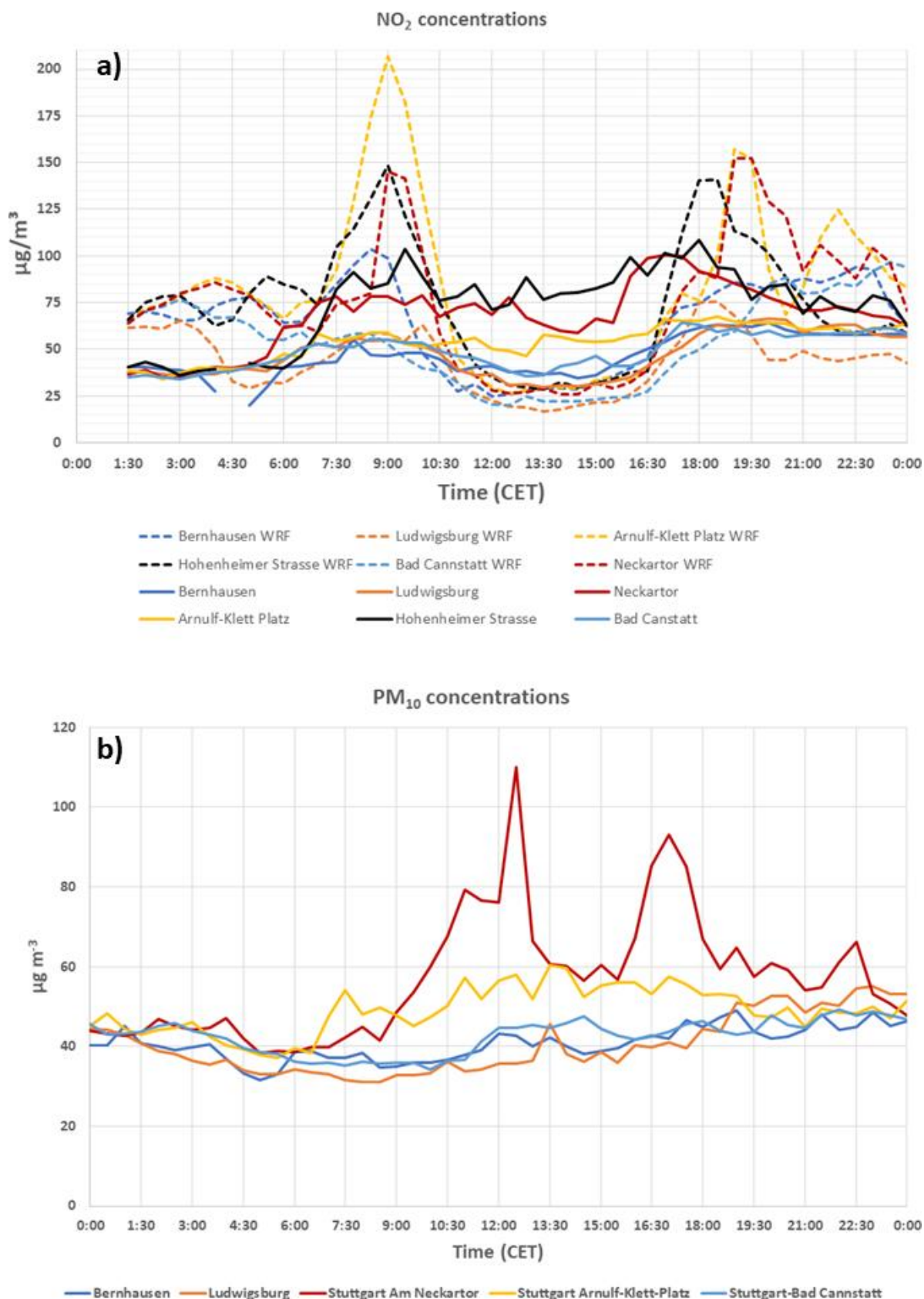


Figure 5: NO₂ (a) and PM₁₀ (b) concentrations at several stations distributed over the model domain on 21 January 2019. The dashed line in (a) denotes the simulated NO₂ concentration and the time zone (CET) corresponds to local time. Measurements at Neckartor, Hohenheimer Strasse, and Arnulf-Klett Platz are directly taken next to the main road.

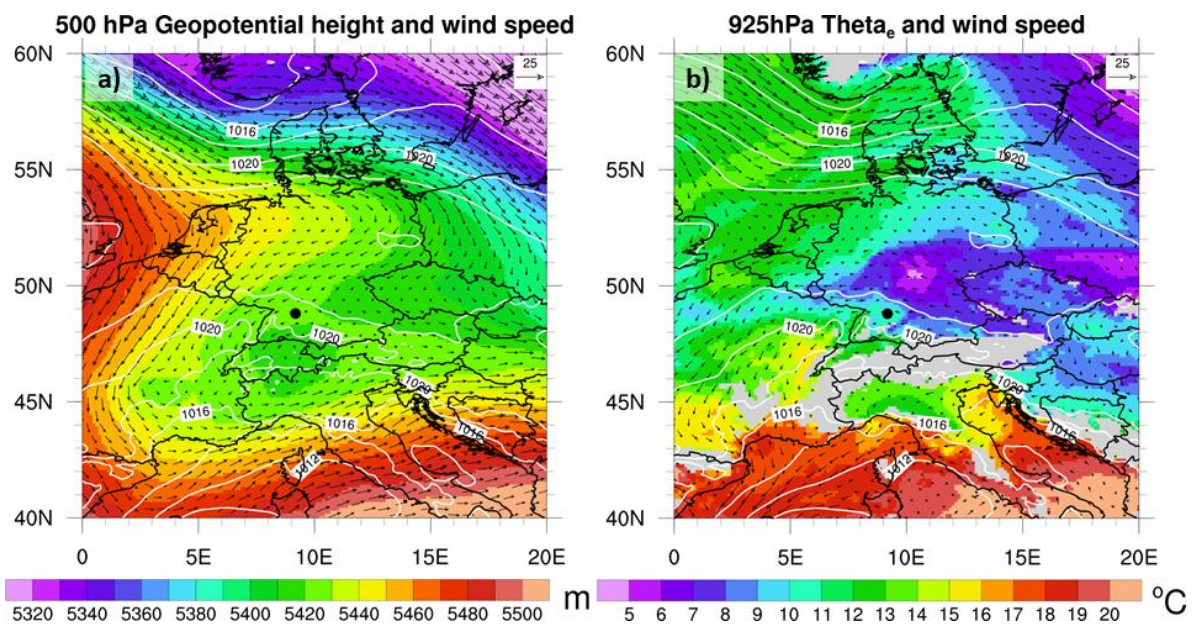


Figure 6: (a) ECMWF operational analysis of 500 hPa geopotential height, sea level pressure (white contour lines) together with 500 hPa wind velocities valid at 00 UTC 21 January 2019. (b) shows the 925hPa equivalent potential temperature together with 925 hPa wind velocities and sea level pressure (white contour lines). Gray areas indicate values below the ECMWF model terrain. The black dot denotes Stuttgart and the reference wind vector length (top right corner of each Figure)) is equal to 25 m s^{-1} .

924

925

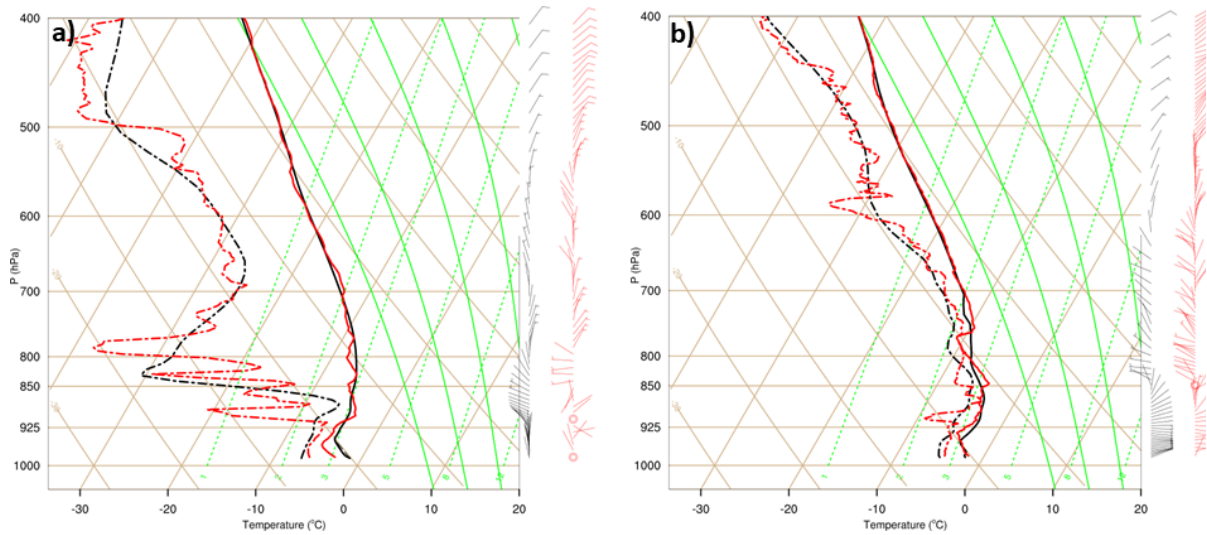


Figure 7: Comparison of temperature, dewpoint and wind of the WRF model simulation (black line) and the sounding from Stuttgart-Schnarrenberg (red line) valid at 00 UTC (a) and 11 UTC (b) 21 January 2019. The solid lines denote the temperature profile and the dash-dotted line denotes the dewpoint profile. Wind barbs denote wind speed in m s^{-1} .

926

927

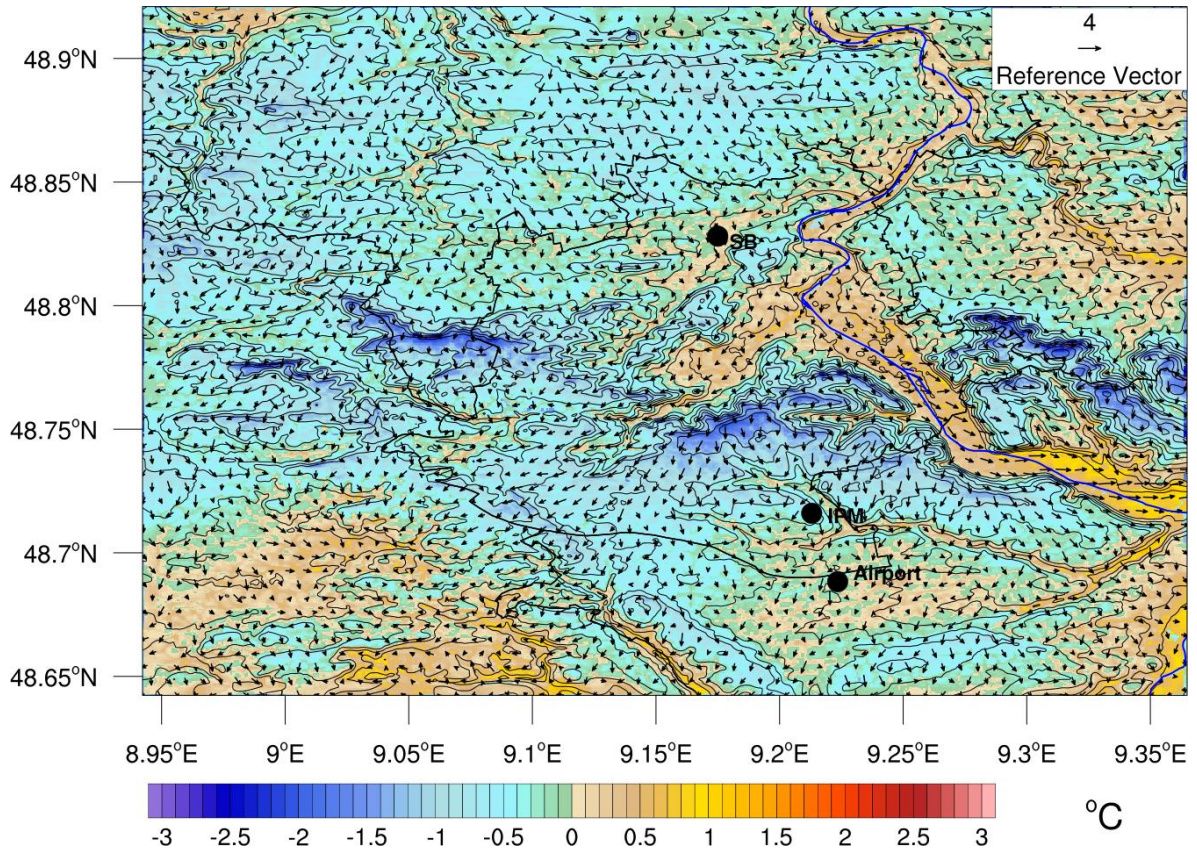


Figure 8: 2-m temperature together with 10-m wind velocities at 12 UTC 21 January 2019. The thick black line denotes the Stuttgart city limits and the thin black contour lines denote the terrain. The blue line denotes the Neckar River (River data © OpenStreetMap contributors 2020. Distributed under a Creative Commons BY-SA License).

928

929

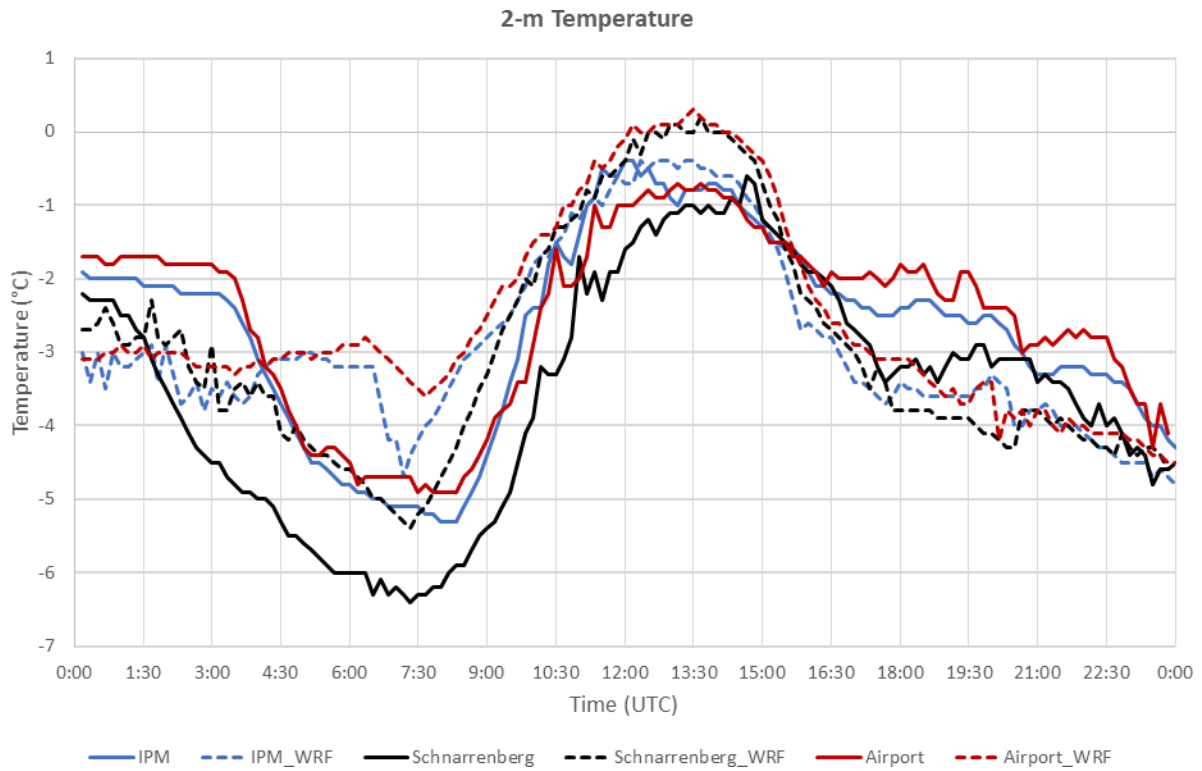


Figure 9: Diurnal cycle of 2-m temperatures for the three meteorological stations shown in Fig. 1b. Solid lines denote the observation, dashed lines denote the model simulation. The temporal resolution of the data points is 10 minutes.

930

931

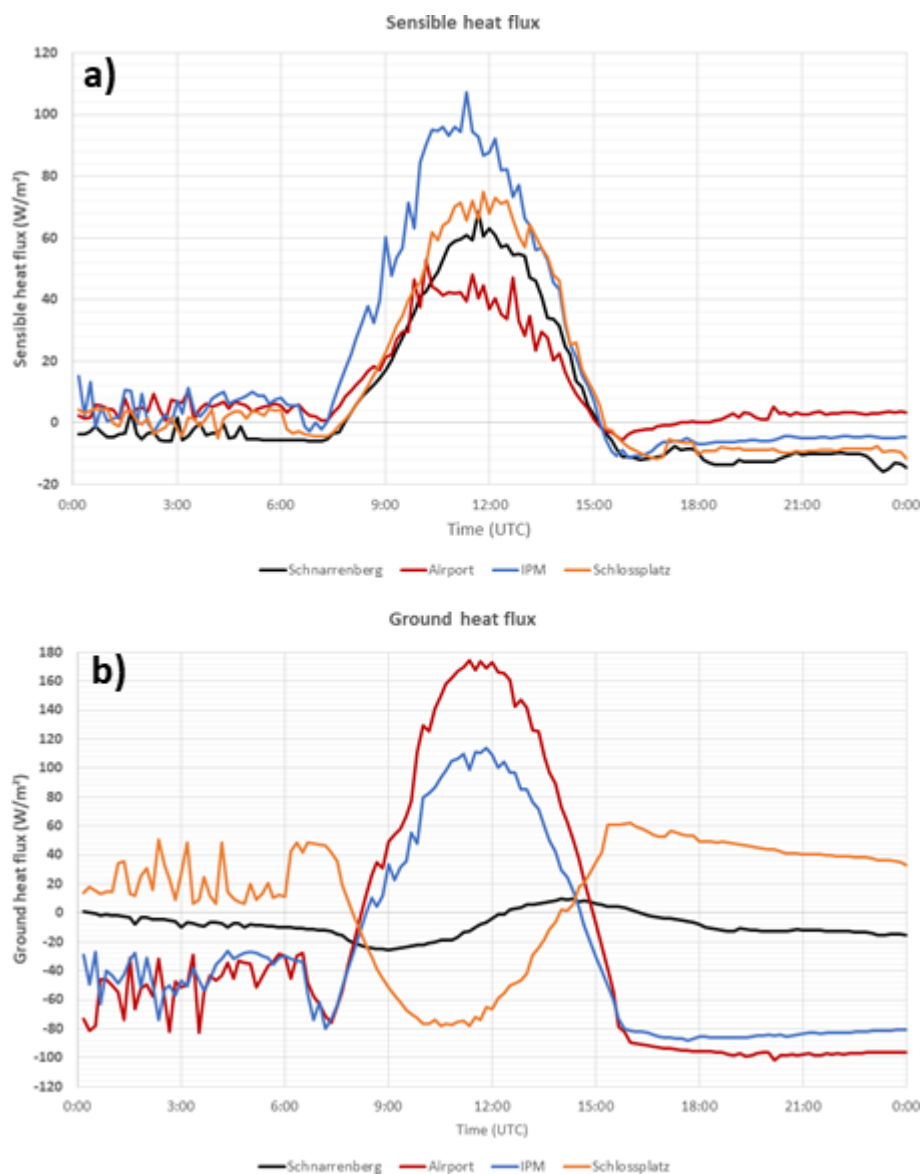


Figure 10: Diurnal cycle of simulated sensible heat flux (SH, a) and ground heat flux (GRDFLX, b) at the four stations Schnarrenberg, Airport, IPM, and Schlossplatz (Fig. 1b). Positive values of GRDFLX indicate fluxes into the soil. The land cover categories are bare soil (airport), croplands (IPM), low-density residential (Schnarrenberg), and high-density residential (Schlossplatz).

932

933

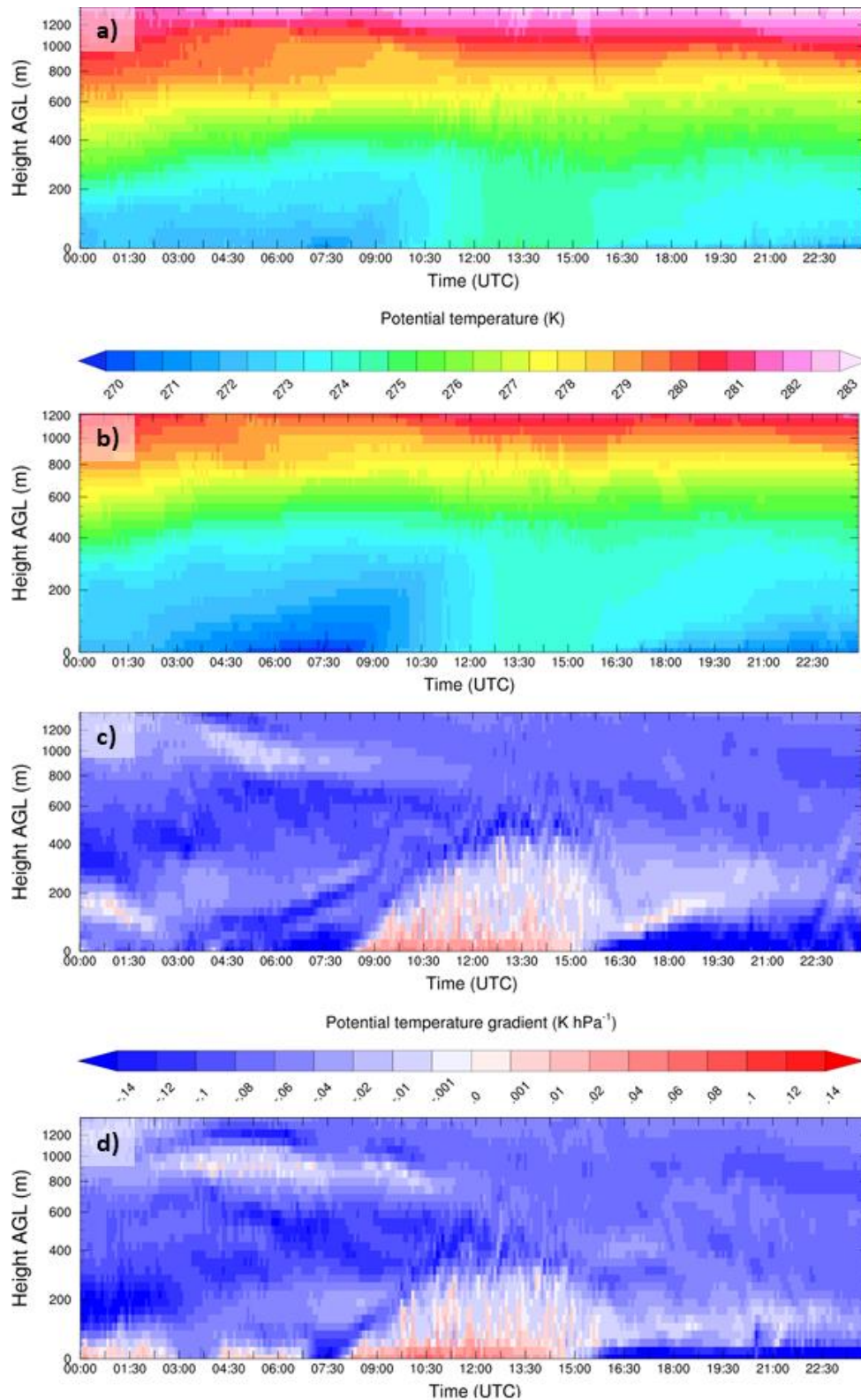


Figure 11: Time-height cross section of the simulated potential temperature at Schnarrenberg (a) and IPM (b). (c) and (d) show the potential temperature gradient at Schnarrenberg (c) and IPM (d). The displayed altitude is above ground level (AGL).

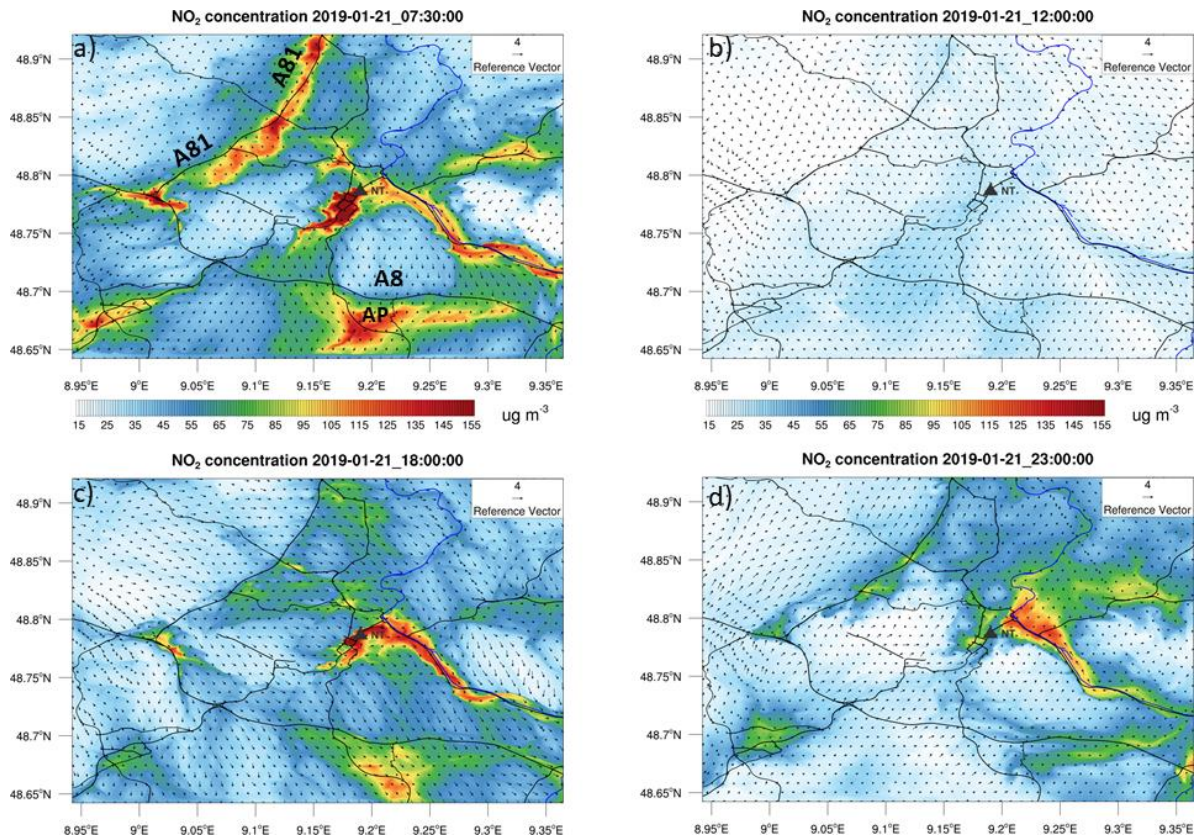


Figure 12: NO₂ concentration at the lowest model level for 07:30 UTC, 12 UTC, 18:00 UTC, and 23 UTC (from a to d) 21 January 2019. The black contour lines denote main roads and motorways in and around Stuttgart (Map Data © OpenStreetMap contributors 2020. Distributed under a Creative Commons BY-SA License). AP denotes the airport, A8 and A81 denote the main motorways around Stuttgart.

935

936

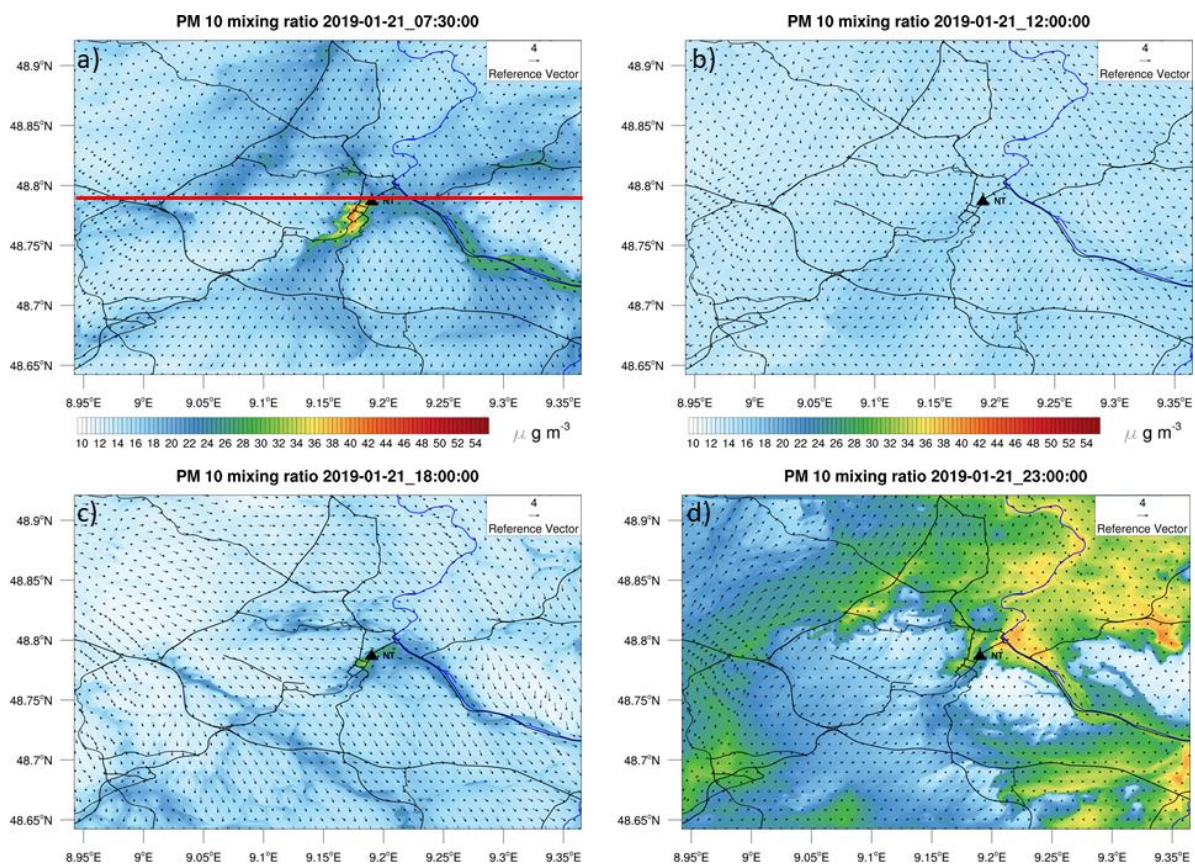


Figure 13: Same as Fig. 12 but for PM₁₀ (Map Data © OpenStreetMap contributors 2020. Distributed under a Creative Commons BY-SA License). The red line in (a) denotes the cross section shown in Figs. 14 and 15.

937

938

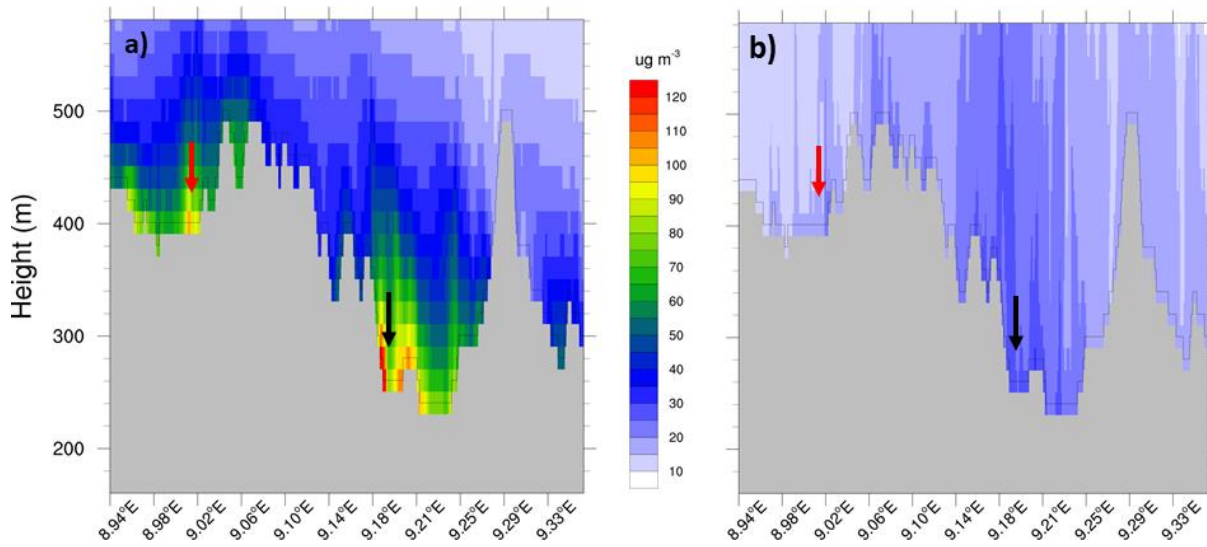


Figure 14: West-East cross section through Neckartor displaying the NO₂ concentration at 07:30 UTC (a) and 12 UTC (b), 21 January 2019. The red arrow denotes the motorway A81 and the black arrow denotes the Neckartor location. The black area shows the model terrain above mean sea level.

939

940

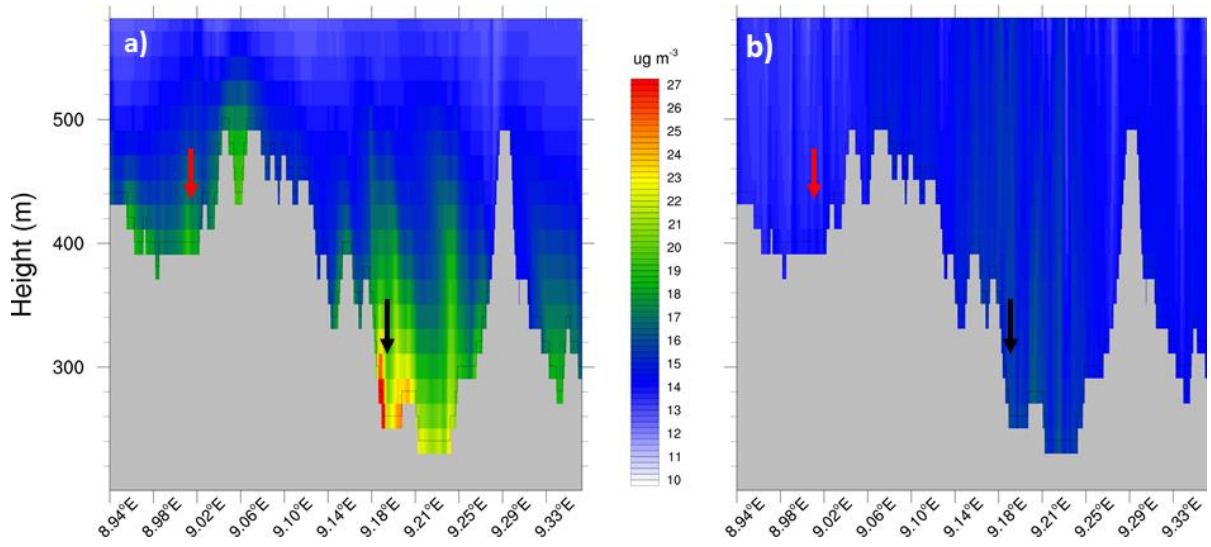


Figure 15: Same as Fig. 14 but for PM₁₀.

941

942

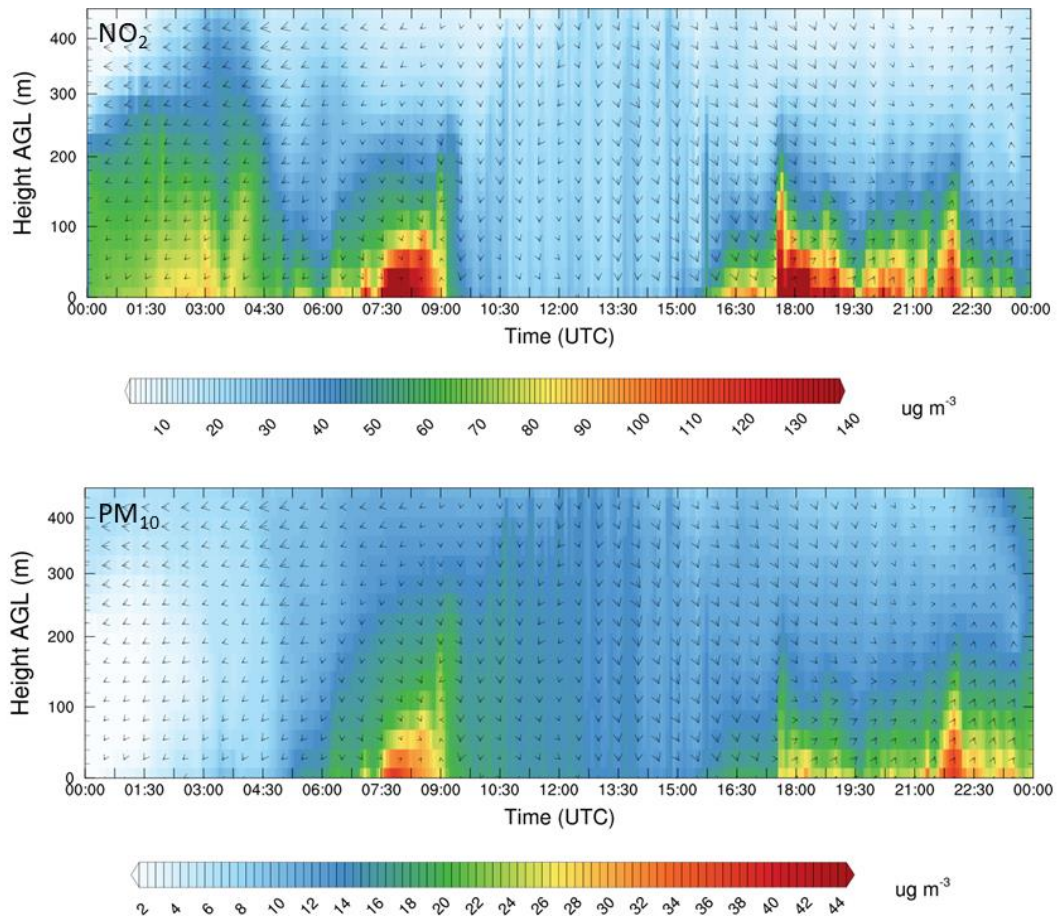


Fig. 16: Time height cross section of NO₂ (top) and PM₁₀ (bottom) at Neckartor (NT) up to an altitude of 450 m AGL.

943